CO_2 and heat energy transport by enhanced fracture permeability in the Monterotondo Marittimo-Sasso Pisano transfer fault system (Larderello Geothermal Field, Italy)

Marco Taussi [1*], Andrea Brogi [2,3], Domenico Liotta [2,3], Barbara Nisi [4], Maddalena Perrini [2], Orlando Vaselli [4,5], Miller Zambrano [6], Martina Zucchi [2]

[1] *University of Urbino Carlo Bo, Department of Pure and Applied Sciences, Via Ca' Le Suore 2/4, Urbino, Italy.*
[2] *University of Bari Aldo Moro, Department of Earth and Geoenvironmental Sciences, Via E. Orabona 4, Bari, Italy.*
[3] *IGG-CNR, Institute of Geosciences and Earth Resources, Via G. Moruzzi 1 - Pisa, Italy.*
[4] *IGG-CNR, Institute of Geosciences and Earth Resources, Via G. La Pira 4, Firenze, Italy.*
[5] *University of Florence, Department of Earth Sciences, Via G. La Pira, 4, Firenze, Italy.*
[6] *University of Camerino, School of Science and Technology, Via Gentile III da Varano 7, Camerino, Italy*

[*] Corresponding author: marco.taussi@uniurb.it

Abstract

Carbon dioxide is one of the most important gases naturally released from geothermal systems. Establishing the processes and pathways that regulate the CO_2 diffuse degassing can provide valuable information for exploration and exploitation purposes of geothermal reservoirs. Areas with high CO_2 emissions are indeed able to reveal major upflow zones from deep reservoirs through deep-reaching permeable fault zones. In this work, a high-resolution CO_2 flux (with records up to 2927 g m^{-2} d^{-1}) and soil temperature (with records up to 98.8 °C) survey was carried out along with detailed fracture parameters measurements in a selected area of the Monterotondo Marittimo-Sasso Pisano transfer fault (Larderello geothermal system, Tuscany, Italy). The main aim was to define the behavior of diffuse CO_2 through the fault system and investigate how the soil CO_2 flux and steam change with respect to the architecture of the fault damage zone (i.e., volumetric fracture intensity, permeability, and persistence of the fractures). The presence of multiple populations of CO_2 flux suggested that three different transport mechanisms control soil degassing: i) purely diffusive, ii) mixed diffusive-advective, and iii) purely advective, characterized by efflux values of <20, between 20 and 300 and >300 g m^{-2} d^{-1}, respectively. The spatial distribution of these fluxes well agrees with the fracture distribution and features of the Jurassic radiolarite (Diaspri Fm) dissected by NNE-striking faults. The interaction between pre-existing fractures and fracture-related fault-zone locally enhances the secondary rock permeability as highlighted by the correlation between Discrete Fracture Network (DFN) modeling and advective flux. Eventually, by normalizing the CO_2 output to the fault strip (1350 m^2), a release of CO_2 equal to ~155 t d^{-1} km^{-2} was estimated.

Key words

Fault zone permeability – CO_2 flux – Steam emission – Larderello geothermal system – Discrete Fracture Network (DFN) – Geothermal exploration

1. Introduction

Carbon dioxide (CO_2) emissions naturally released from geothermal systems, and more generally from natural systems, are a timely theme object of scientific debates in the frame of natural vs. anthropogenic contribution of greenhouse gases, with the former being by far the most significant ones (e.g., Fischer and Aiuppa, 2020). However, while anthropogenic CO_2 emissions can be evaluated relatively easily, more difficult is the estimation of the amount of CO_2 naturally escaping from Earth's surface (Bertani and Thain, 2002). Different methodologies such as remote sensing (e.g., ground-based and air- and space-borne techniques; Queißer et al., 2019 and references therein) and in-situ (e.g., eddy covariance, accumulation chamber, and dynamic concentration methods, e.g., Parkinson, 1981; Chiodini et al., 1998; Camarda et al., 2006, 2009, 2019; Lewicki and Hilley, 2009) measurements are commonly adopted to determine the flux of CO_2 escaping from the ground.

In the last decades, CO_2 flux measurements were carried out in several geothermal sites worldwide such as Brady's (USA; Jolie et al., 2015, 2016), Ohaaki, Taupo, and Rotorua (New Zealand; Werner and Cardellini, 2006; Rissmann et al., 2012), Los Humeros (Mexico; Peiffer et al., 2018; Jentsch et al., 2020), Furnas (Azores; Viveiros et al., 2010; 2020), Copahue, Cerro Blanco, Cordón de Inacaliri and Cerro Pabellón (Argentina and Chile; Chiodini et al., 2015; Lamberti et al., 2019, 2021; Taussi et al., 2019, 2021), Yangbajain (Tibet; Chiodini et al., 1998), Reykjanes, Hengill and Krýsuvík (Iceland; Fridriksson et al., 2006; Hernandez et al., 2012; Gudjónsdóttir et al., 2020), Latera, Mount Amiata, Torre Alfina (Italy; Chiodini et al., 2007, 2020; Nisi et al., 2014; Carapezza et al., 2015; Sbrana et al., 2020), among the others.

Despite the increasing efforts to provide precise estimates of CO_2 diffusing from geothermal (and volcanic) areas a lot of work is to be done before achieving a realistic output of CO_2 from these sources. Moreover, CO_2 measurements allow computing, though partially, the total CO_2 output from geothermal sites, since even extensive surveys are not able to entirely cover the areas due to large territories to be explored, uneven grounds, and the presence of dangerous sites such as e.g. mofette, hot pools and free gas discharges that might prevent reliable measurements. In addition, CO_2 emissions are subject to temporary (seasonal or permanent) changes linked, for example, to the variation of (i) atmospheric parameters (e.g., Klusman et al., 2000; Lelli and Raco, 2018; Delsarte et al., 2021), (ii) hydrothermal or volcanic system dynamics (e.g., Pérez et al., 2012; Werner et al., 2016; Cardellini et al., 2017); (iii) geothermal power plants operations (e.g., Bertani and Thain, 2002; Frondini et al., 2009; Rissmann et al., 2012; Fridriksson et al., 2017; Manzella et al., 2018; Jentsch et al., 2021), and (iii) transient permeability (e.g. Camarda et al., 2009). Although these limitations, measurements of natural CO_2 degassing are facilitated when the structural setting is known. Fluid circulation at high-to-moderate temperature as well as CO_2 escape is generally controlled by structural conduits in fault damage zones (e.g., Sibson, 2000; Fairley and Hinds, 2004; Rowland and Sibson, 2004; Lewicki et al., 2005; Werner and Cardellini, 2006; Anderson and Fairley, 2008; Faulkner et al., 2010; Faulds et al., 2011; Jolie et al., 2016; Lamberti et al., 2019; Barcelona et al., 2020), where fracture spacing, attributes (e.g., orientation, length, height, aspect ratio, intensity, and aperture), and distribution can strongly enhance permeability (Caine et al., 1996; Caine and Forster, 1999; Billi et al.; 2003; Agosta et al.; 2010; Cox et al., 2001; Zucchi et al., 2017, 2022). These attributes can be used for creating Discrete Fracture Network (DFN) models as representations of the natural fracture network (Lucia, 1999; Nelson, 2001, Kim et al.; 2004). Conventional DFN methods assume that flow and transport are controlled by the fracture network, neglecting the participation of the rock matrix. Consequently, the obtained models can be used intrinsically or upscaled into an equivalent continuous model encompassing the hydraulic properties (e.g., permeability) of the fracture network (Hadgu et al., 2017). Thus, considering that CO_2 emissions are mainly concentrated along fault zones (Curewitz and Karson, 1997; Jolie et al., 2016; Taussi et al., 2019, 2021; Lamberti et al., 2019; Jentsch et al., 2020), their geometrical reconstruction can offer the best opportunity to study CO_2 emission pathways, secondary mechanisms (e.g., reduction-oxidation processes of C-bearing species), and outputs along key transects across the fault zone under study.

In this paper, we present and discuss the results of a high-resolution soil CO_2 flux measurements coupled with soil temperatures, combined with the measurements of fracture parameters and DFN modeling along a fault zone crossing the worldwide famous Larderello geothermal area (Italy) in its peripheral zone (Monterotondo Marittimo-Sasso Pisano area, hereafter MMSP; Fig. 1), where CO_2 emissions are accompanied by noticeable steam escaping. This fault zone, at least 5 km long, is part of a km-scale NE-oriented brittle shear zone, interpreted as part of a regional transfer zone (Gola et al., 2017; Liotta and Brogi, 2020) developed in the framework of the Neogene-Quaternary extensional tectonics affecting the inner Northern Apennines (Carmignani et al., 1994; Liotta et al., 1998; Brogi et al., 2005; Barchi, 2010).

The main goals are to i) verify the behavior of the diffused CO_2 and steam through the fault system; ii) investigate how the diffuse CO_2 fluxes and steam change with respect to the volumetric fracture intensity, permeability, and persistence of the fractures; iii) compute the total CO_2 output of the study area, comparing it with other geothermal areas.

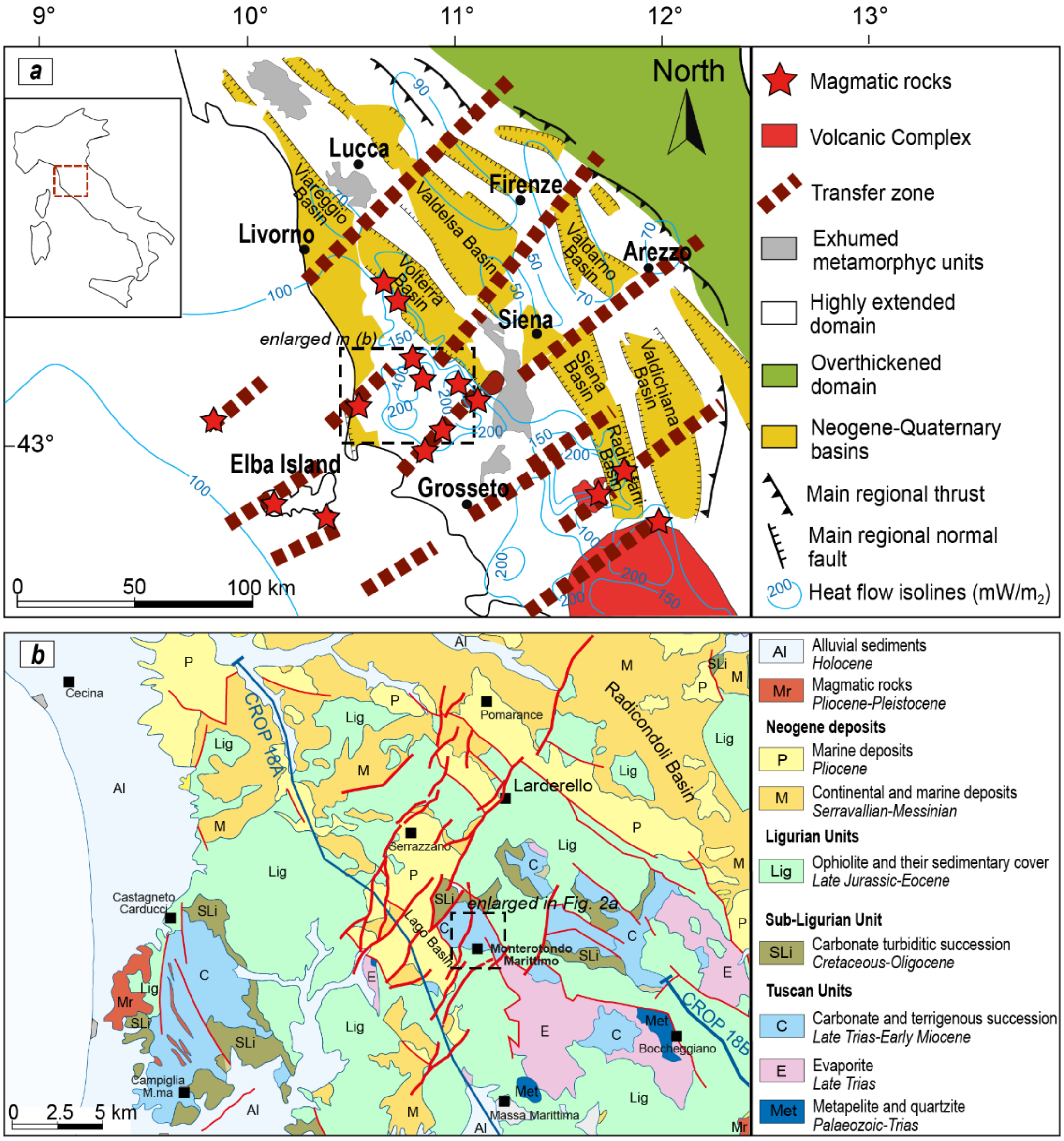

Figure 1. a) Structural sketch map of the Northern Apennines and Northern Tyrrhenian Sea; b) geological map of the Larderello area (modified after Liotta and Brogi, 2020). The study area is highlighted by the black dashed frame.

2. Geological background of the Larderello area

The Larderello geothermal area is a magmatic-driven geothermal system (Baldi et al., 1994; Bellani et al., 2004; Gola et al., 2017; Rochira et al., 2018) located in the inner Northern Apennines (Fig. 1a), a NE-verging Alpine belt (Vai and Martini, 2001) which experienced convergence and collisional processes (Cretaceous-early Miocene) and subsequent extension since early-middle Miocene (Carmignani et al., 1994). One of the clearest indications of the collisional process is given by high-pressure metamorphism (up to 1.5 GPa, Theye et al., 1997; Brunet et al., 2000; Rossetti et al., 2002; Bianco et al., 2019) developed during the eastward stacking of the tectonic units deriving from the oceanic (Ligurian units, *Auctt.*), transitional (Sub-Ligurian units, *Auctt.*) and continental (Tuscan Nappe, *Auctt.*) paleogeographic domains of Northern Apennines (Molli, 2008). The subsequent eastward migration of the extensional tectonics resulted in: (a) Miocene lateral segmentation of the previously stacked units (Brogi, 2004; Brogi et al., 2005; Brogi and Liotta, 2008); (b) development of

Pliocene-Quaternary NW-striking normal faults cross-cutting all the previous structures and inducing NW-trending tectonic depressions, filled by continental and marine sediments (Martini and Sagri, 1993; Brogi, 2020; Martini et al., 2021). The primary evidence of extension is the opening of the Tyrrhenian Basin (Bartole, 1995) and the present crustal and lithospheric thickness of about 20 and 40 km, respectively (Calcagnile and Panza, 1980; Locardi and Nicolich, 1988; Di Stefano et al., 2011; Moeller et al., 2013). At least since the Langhian, extension was accompanied by eastward migrating magmatism (Serri et al., 1993), affecting the Tuscan archipelago and the inland inner Northern Apennines (Serri et al., 2001; Dini et al., 2005, 2008). Magmas were emplaced at shallow crustal levels (mainly at 6–8 km depth; Serri et al., 2001) mostly along the NE-striking brittle shear zones (Dini et al., 2008; Spiess et al., 2021 and references therein), which played the role of transfer zones in the inner Northern Apennines (Liotta, 1991; Dini et al., 2008) and lateral ramps in the outer Northern Apennines (Liotta, 1991), where coeval compression occurred (Elter et al., 1975). Currently, no active volcanoes are present in Tuscany although heat flux is 120 mW/m^2 on average (Della Vedova et al., 2001; Pauselli et al., 2019). However, local peaks up to 1000 mW/m^2 were estimated in the Larderello geothermal area (Baldi et al., 1994; Della Vedova et al., 2001), which is located along one of the most relevant transfer zones crossing the Northern Apennines (Fig. 1a) that hosts a Pliocene-Pleistocene pull-apart-like tectonic depression named Lago Basin (Fig. 1b). The latter developed above a cooling magma localized at depth. The geothermal fluid flow is particularly active (Gola et al., 2017; Rochira et al., 2018; Liotta and Brogi, 2020), contributing to determin the bulk of the electricity production of the Larderello geothermal field (Barbier, 2002; Romagnoli et al., 2010).

The tectonic and stratigraphic units occurring in the Larderello area have been described by several authors (e.g., Lazzarotto, 1967; Lazzarotto and Mazzanti, 1978; Costantini et al., 2002; Elter and Pandeli, 1990; Pandeli et al., 1991, 1994; Dini et al., 2005; Bertini et al., 2006; Brogi and Cerboneschi, 2007; Romagnoli et al., 2010). Concerning the MMSP area (Fig. 2), the carbonate, siliceous and terrigenous successions of the Tuscan Nappe are broadly exposed, surrounded by the Ligurian and Sub-Ligurian Units.

Information from deeper structural levels derive from deep boreholes drilled during the geothermal exploration and exploitation (Bertini et al., 1991; 2006; Romagnoli et al., 2010), and interpretation of reflection seismic lines. They display the occurrence of a high-impedance seismic reflector, named as K-horizon (Batini et al., 1978; Cameli et al., 1993), ranging in depth between 3 and 7 km, and considered as an active shear zone, located at the top of the brittle-ductile transition (Cameli et al., 1993, 1998; Liotta and Ranalli, 1999; De Matteis et al., 2008), possibly hosting fluids at supercritical conditions (Agostinetti et al., 2017). The K-horizon shows a dome-shaped culmination West to the MMSP area, in correspondence with the Lago Basin (Liotta and Brogi, 2020 and references therein). Here, the highest values of heat flow (Baldi et al., 1994; Della Vedova et al., 2001), and relatively high $^3He/^4He$ isotopic ratios (Magro et al., 2003) were measured, suggesting that the Lago Basin is a preferential area for mantle-derived fluids escaping. The study area is in the shoulders of this basin, where the substratum of the Neogene deposits crops out (Fig. 1b), and the natural CO_2 emissions are located.

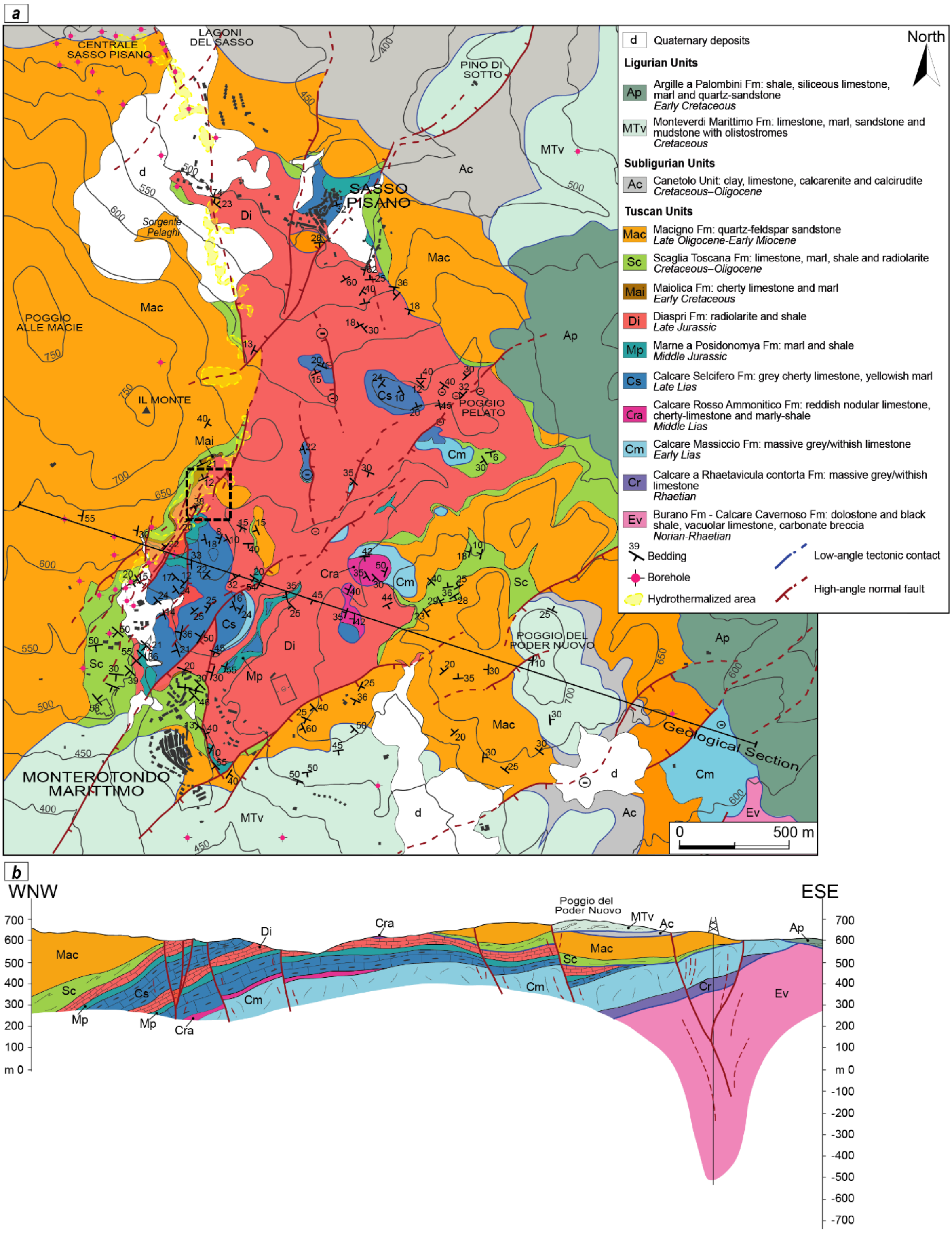

Figure 2. a) Geological and structural map of the Monterotondo Marittimo-Sasso Pisano (MMSP) area in which the main faults defining the transfer zone and the study area (black dashed frame) are shown; b) geological section across the study area. Its trace is indicated in (a).

3. Hydrothermal manifestations

Le Biancane natural park comprehends some of the numerous areas characterized by hydrothermally altered surfaces that occur between Monterotondo Marittimo and Sasso Pisano villages which extend from <1,000 up to >40,000 m^2 (Fig. 3). Alteration and kaolinization produced the typical bleaching process, which mainly involves the marly-clay and siliceous lithotypes, whereas Fe-oxides and hydroxides developed on the terrigenous succession of the Tuscan Domain (Orlandi, 2006; Bentivegna, 2010; Regione Toscana, 2014).

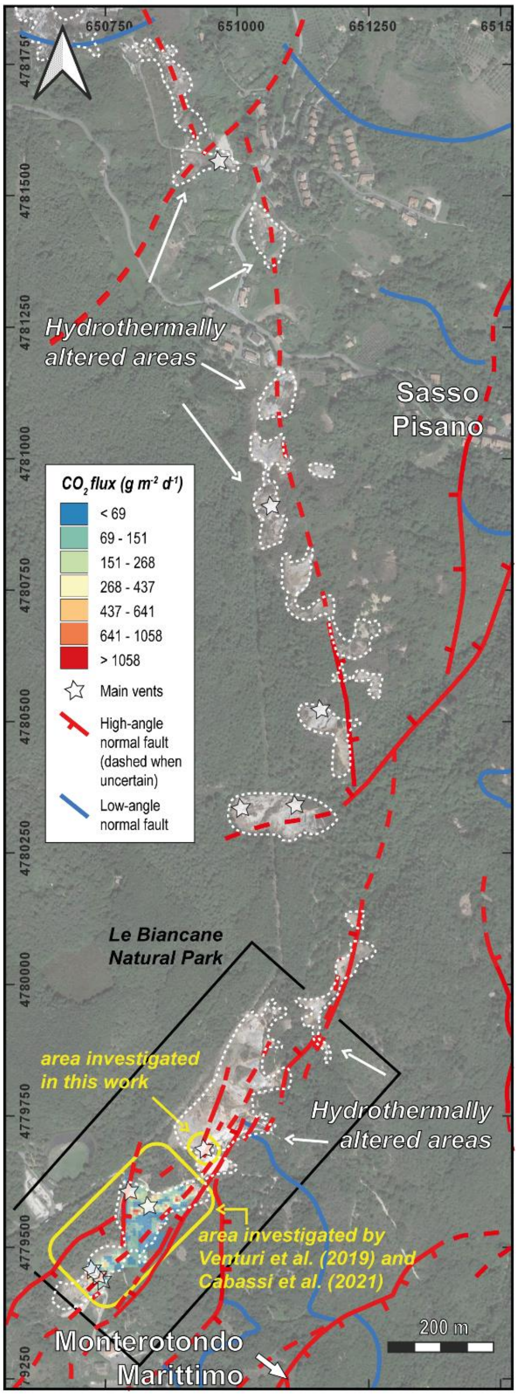

Figure 3. Hydrothermally altered zones along the Monterotondo Marittimo-Sasso Pisano fault zone. The location of the main faults and hydrothermal vents (after Venturi et al., 2019; Leila et al., 2021; maga database www.magadb.net) are also reported and the diffuse soil CO_2 measurements by Venturi et al. (2019) and Cabassi et al. (2021) are highlighted.

Geothermal manifestations along the MMSP fault zone consist of fumaroles, steam vents, acidic and boiling steam-heated pools, and mud pools called “lagoni” (e.g., Duchi et al., 1986, Minissale, 1991; Duchi et al., 1992) (Fig. 4). At the fumarole vents, acicular aggregates or encrustations of native sulfur are commonly found (Fig. 4), sometimes in association with gypsum and other sulfate and borate minerals (Orlandi, 2006; Bentivegna, 2010).

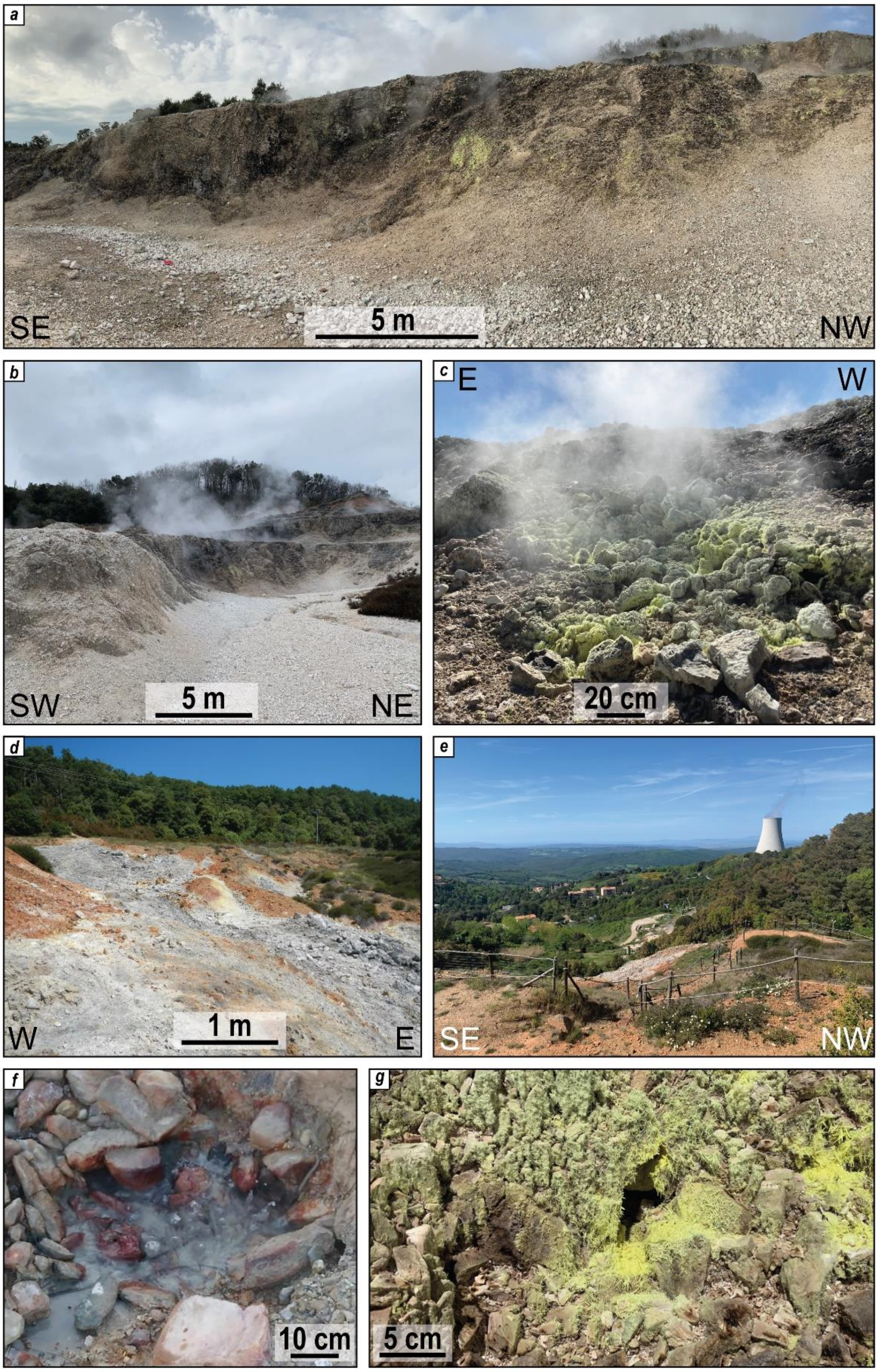

Figure 4. Field photographs from the *Le Biancane* natural park. a-b) wall of an abandoned quarry with visible fumaroles and steaming grounds; the rock scarp crosscuts the Monterotondo Marittimo-Sasso Pisano fault zone; c) fumarolic manifestations; d) hydrothermally altered grounds; e) panoramic view of the park with a geothermal power plant cooling tower in the background; f) bubbling pool; g) acicular aggregates and encrustations of native sulfur in a fumarolic vent.

The discharged fluids are mostly at the water boiling temperature and are dominated by H_2O (>95% v/v) followed by CO_2, N_2, H_2S, H_2, and CH_4, with minor amounts of O_2 and noble gases (Scandiffio et al., 1995; Magro et al., 2003; Venturi et al., 2019; Leila et al., 2021). The fumarolic fluids at Sasso Pisano show $^3He/^4He$ (as R/Ra) isotopic ratios up to 2.32 (Hooker et al., 1985) suggesting mixing processes, at variable degrees, between mantle (up to 40% when considering the MORB as representative of the mantle beneath Tuscany; Hooker et al., 1985) and crustal fluids (Magro et al., 2003). The R/Ra value at Sasso Pisano is higher than the one measured in the Lago fumaroles (i.e., 1.63; Minissale et al., 1997) but lower than the maximum value recorded in the geothermal wells (i.e., up to 3.2; Hooker et al., 1985). The isotopic composition of Carbon in CO_2 (expressed as $\delta^{13}C$-CO_2) from the Monterotondo Marittimo fumaroles ranges from −4.2 to −2.4‰ vs V-PDB (Venturi et al., 2019; Leila et al., 2021), and is similar to those recorded in the fluids discharging at Sasso Pisano (from −3.83‰ up to −2.3‰ vs V-PDB; Minissale et al., 1997; Tassi et al., 2012; Leila et al., 2021). The $\delta^{13}C$-CO_2 values are in the isotopic range observed for other fumaroles (e.g., from −7.26 to −0.26‰ vs V-PDB; Minissale et al., 1997) and geothermal wells (from −7.1 to −1.4‰ vs V-PDB; Gherardi et al., 2005) of the Larderello geothermal system. The isotopic data account for a CO_2 dual source (Gherardi et al., 2005), i.e. (i) magmatic degassing (i.e., −8 to −4‰ vs V-PDB; Mason et al., 2017) and (ii) decarbonation of carbonates and calc-silicates (i.e., −5 to +5‰ vs V-PDB; Venturi et al., 2017 and references therein).

Diffuse degassing of soil CO_2, $\delta^{13}C$-CO_2 in interstitial gas, soil temperatures and gaseous elemental mercury (GEM) emissions were measured in a selected area of about 20,000 m^2 within the *Le Biancane* natural park, located just 100 m SW from the study area (Fig. 3), by Venturi et al. (2019) and Cabassi et al. (2021) during the summer season. These authors measured CO_2 fluxes ranging from <2 up to 2,144 g m^{-2} d^{-1} linked to soil temperature from 27.1 to 94.5 °C, the latter also in agreement with those measured by Silvestri et al. (2020) through remote sensing. The soil CO_2 fluxes showed no spatial correlation with soil temperature, nor with GEM emissions, which were ranging from below the detection limit up to 0.65 μg m^{-2} d^{-1} (Cabassi et al., 2021). Noteworthy, these authors also evidenced the presence of microbiological activity in the hydrothermally altered soils, suggesting that it plays an important role in both governing the, CO_2, CH_4 and GEM emission and affecting the $\delta^{13}C$-CO_2 composition of the interstitial gas, the latter showing a general enrichment in ^{13}C ($\delta^{13}C$-CO_2 up to +3.41‰ vs V-PDB) with respect to the carbon isotopic signature of the fumaroles.

4. Methods

The relationships among fractures, CO_2 flux and heat escaping from the soil were reconstructed through geochemical and geological surveys that have been carried out in selected areas of the *Le Biancane* natural park (Fig. 3).

4.1 Soil CO_2 flux and temperature measurements

In July 2021, 75 soil temperature and CO_2 flux measurements were taken with stable weather conditions and dry soils in the selected fault zone crossing the study area using the accumulation chamber method (e.g., Chiodini et al., 1998, Carapezza and Federico, 2000; Cardellini et al., 2003; Viveiros et al., 2010, 2020; Nisi et al., 2013; Lamberti et al., 2019; Taussi et al., 2021). Each measurement lasted about 2-3 minutes and the entire survey was completed in about 4 hours. No major changes in barometric pressure and air temperature were recorded during the survey, as they ranged between 940 and 945 mbar and 25 and 30 °C, respectively. The measurement campaign was carried out following as much as possible a regular grid of about 4 x 4 m over a restricted area of 1350 m^2 (0.00135 km^2). However, the spatial distribution of the diffuse CO_2 soil gas and temperature spots was partly influenced by the presence of uneven grounds and compact hard rocks which led to some irregularities of the grid. Each node was located with a portable GPS Garmin GPSmap 62st. In order to maintain the trajectories as much linear as possible, benchmarks and a measuring wheel were also used in the field. Next to each soil CO_2 sampling point, soil temperatures were measured using a TERSID thermocouple (dynamic range from −20 to 1150 °C; uncertainty ± 0.1 °C; Tassi et al., 2016) inserted slightly below the ground to avoid the interference due to the wind. The accumulation chamber equipment consists of a cylindrical metal vase (the chamber), a Licor® Li-820 infrared spectrophotometer, an analogical-digital converter, and a palmtop computer. The chamber has a basal area of 200 cm^2 and an inner volume of 3060 cm^3 and is equipped with a ring-shaped perforated collector connected to a low-flow pump (20 $mL \cdot s^{-1}$). The pump permits to convey the soil gas from the chamber to the spectrophotometer and the re-injection of the circulating gas into the chamber guarantees the mixing of the soil gas by also minimizing the effect produced by the pumping action. The infrared detector has a sensor operating in the range of 0-20,000 ppm of CO_2 with an accuracy of 4%. The signal is transformed by the analogical-digital converter and transmitted to the palmtop computer equipped with the Palm Flux 5.36 software, where a CO_2 concentration vs. time diagram is plotted in real-time. The instrument used in this work has a detection limit of ~0.08 g m^{-2} d^{-1} (https://www.westsystem.eu/it) and was calibrated before the fieldwork utilizing a laboratory calibration curve. The latter allowed to convert the temporal variation of the CO_2 concentration inside the chamber ($dC_{CO2}\ dt^{-1}$, expressed in ppmV/s), into the CO_2 flux (ϕCO_2, expressed in g m^{-2} d^{-1}), through a correlation factor (*cf*) obtained from the slope of the linear best-fit line of ϕCO_2 vs $dC_{CO2}\ dt^{-1}$. The measured ϕCO_2 was thus computed according to the following equation (e.g., Tassi et al., 2013; Cabassi et al., 2021):

$$\phi CO_2 = cf\ \times dC_{CO2}\ dt^{-1}$$

4.2 CO_2 and temperature data processing, spatial distribution, and CO_2 output estimation

The CO_2 flux and temperature data were processed using statistical and geostatistical methods to explore their spatial distribution and the origin of the CO_2 diffuse emission. The data were analyzed by using the Graphical Statistical Analysis (GSA) method (Chiodini et al., 1998), according to the procedure proposed by Sinclair (1974). The presence of multiple sources results in a polymodal distribution of the values, displaying a curve with one or more inflection points on a probability plot. The GSA method consists of the subdivision of these distributions into individual populations characterized by different proportions in the dataset, mean and median values, and standard deviations.

The distribution maps of both soil CO_2 flux and temperature were constructed using the log-normal Kriging interpolation method (e.g., Krige 1951; Matheron, 1970) using the Isatis© software package of Geovariances. The methodology involved the realization of an experimental variogram and the selection of the best fitting mathematical model for each variable. The fitted models were then cross-validated with the experimental data to check the performance of the model for kriging. The maps were then graphically reported using the QGIS software.

The total CO_2 output was calculated by applying the Sichel's t-estimator (Mi) (David, 1977). The estimation was derived by multiplying Mi times the area covered by the population. In the same way, the central 95% confidence intervals of the CO_2 output were used to calculate the uncertainty of the populations.

4.3 Field work and Discrete Fracture Network modelling

A new field mapping of about 10 km^2 at a 1:5000 scale (Fig. 2) and collection of structural data in the most favorable exposures were carried out to obtain information on the geological and structural setting of the study area. Furthermore, looking at the area where the geothermal manifestations are concentrated, fracture distribution across the fault zone, was investigated to reconstruct the interplay among brittle deformation, fracture enhancement, and gas escaping. In particular, a detailed analysis of the fracture distribution was carried out in a key outcrop where highly fractured and hydrothermally altered Jurassic siliceous beds (Diaspri Fm, Tuscan Domain) are exposed in an abandoned quarry within *Le Biancane* natural park (Figs. 2 and 5).

In the field, fracture parameters (orientation, length, linear fracture intensity, mechanical aperture) were obtained through the scanline and scan area methodology. Most data were collected along a 25 m long scanline crossing the main wall of the abandoned quarry where the fault zone is clearly visible (Fig. 5). To increase statistical significance of the data in terms of variability and spatial distribution, six additional (secondary) scanlines (SL A to F in Fig. 5), 1-2 m long each, were also performed: four scanlines were located at the same scarp of the main scanline (N145° oriented); the other two scanlines were settled in an adjacent scarp (N80° oriented) at about 30-40 m NW from the main scanline. Five scan areas (~1-2 m^2) were performed on the few pavement views allowing the measure of the fracture network in plain view (SL B and G in Fig. 5). Due to their mutual proximity, four scan areas result in a single point in Figure 5. corresponding to SL G. The length of the secondary scanlines can be considered sufficient on the basis of the high fracture intensity (Wei et al., 1996) and the near constant fracture spacing (7-10 cm) measured in the field. The location of the scanlines was chosen with respect to the variability of fracture intensity and the availability of outcrops not affected by hydrothermal alteration. This latter indeed inhibits the analyses of the fracture networks.

The first step of our fracture analysis consisted of clustering the fracture network in different sets, according to their orientation. Since most fractures observed in the field are about normal to bedding, the fracture clustering was evaluated also considering the fracture setting after having reported bedding to its horizontal attitude (e.g., Labeur et al., 2021), independently by the cause that determined the bedding rotation. For each fracture set, the mean orientation (azimuth, dip) and the Fisher's K dispersion parameter (Fisher, 1953), required for the modelling, were calculated. Low Fisher's K values (K < 50) imply that the fracture cluster has a high dispersion of dip/azimuth orientations, whereas high values (K > 200) indicate that the dip/azimuth orientations are more uniform and homogenous within a fracture cluster. For the DFN modeling, all fracture families were modeled considering the current orientation measured in the field.

The fracture length (defined as the trace of the fracture on the bedding plane) distribution for each family was derived by the analysis of the pavements scan areas. Similarly, the fracture height (defined as the trace of the fracture on a vertical view) distribution was obtained from the scanlines performed on the walls. The aspect ratio (length/height) was estimated by considering the average of both properties. Considering the limited useful exposures, in some cases the length distribution was affected by truncation and censoring effects (not included in the models), described as the underestimation of small fracture population and the incomplete observation of long fractures (i.e., those longer than the outcrop), respectively (Bonnet et al, 2001). The volumetric fracture intensity (*P*32, defined as the total surface area of fractures planes per unit of volume) was derived by using the simulation-based workflow, proposed by Golder Associated Ltd. (2009) and already applied by other authors (e.g., Antonellini et al., 2014; Korneva et al., 2015; Zambrano et al., 2016). This approach is based on the linear relationship between the *P32* and the *P10* (linear fracture intensity). The method consists in generating a series of preliminary DFN models with fixed fracture parameters (orientation, length distribution, aspect ratio) and variable input volumetric intensity (*P*32). For each inputted *P32* value, a *P10* corresponding value is obtained by dividing the number of fractures intersecting a pseudo-well by the length of the pseudo-well normal to the fracture set (Terzaghi, 1965). It is recommended to use at least three models (including several pseudo-scanlines with different orientations) with different input *P32* values to check the trend consistency and the regression line (e.g., Zambrano et al. 2016). Eventually, the ratio *P32/P10* is obtained by linear regression (Dershowitz and Herda, 1992).

The hydraulic aperture, *e* (defined as the idealized fracture aperture for smooth parallel plates model; Snow, 1965), depends on the relative displacement of the opposite fracture walls (mechanical aperture) and their roughness (Zambrano et al., 2019). Here, the hydraulic aperture was derived from the mechanical aperture (*E*) and the Joint Roughness Coefficient (JRC), by using the equation of Barton et al. (1985):

$$e = \frac{E^2}{JRC^{2.5}}$$

The JRC parameter was measured by visually comparing the fracture surface with a standard set of roughness profiles given by Barton and Choubey (1977). The mechanical aperture (*E*) of fractures was measured using a comparator with an accuracy of 0.01 mm.

Finally, stochastic DFN models were built using MOVE™ software of Petroleum Experts® by introducing the parameters derived from the field analysis: i) orientation; ii) fracture length; iii) aspect ratio; iv) aperture. The DFN models (35 x 48 x 3 m, with the largest size oriented N330º, and one-meter cell size) were generated to represent the documented fracture network (Fig. 5), computing both fracture porosity and geometric-based permeability tensor (Oda, 1985). Since most of the fractures crossing the chert beds are not vertically connected, a hybridization of the model was made to introduce the rhythmically interbedded shaly levels, assuming for the latter an estimated permeability of 10^{-17} m^2 and a near 20% of the total thickness. To do that, the vertical component of the permeability was averaged using the weighted harmonic mean between both lithofacies (i.e., cherts and shaly levels), whereas the arithmetic mean was used for the horizontal components (Antonellini et al., 2014). The contribution of the permeability associated with fault parallel non-stratabound fractures located in the proximity (0.5 m) of the fault surface was not affected by this upscaling, due to the tendency of these fractures to cross the first mechanical boundary (bedding). The results of cells along the main vertical wall were extracted to compare the fracture parameters (i.e., fracture intensity, porosity, and permeability) with the output of the geochemical survey (i.e., soil temperature and CO_2 natural emissions).

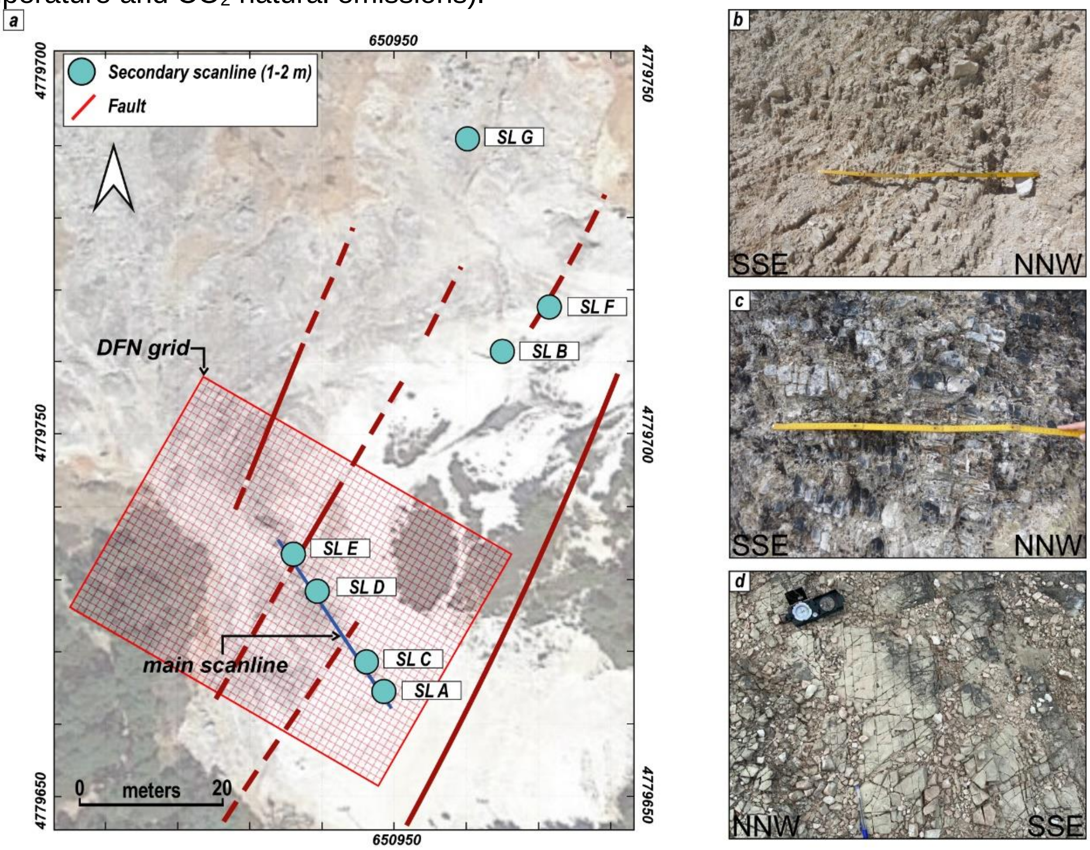

Figure 5. a) Map showing location of scanlines, DFN grid and the main faults affecting the area. The grid of the DFN model was oriented to follow the main orientation (N30°) of the observed faults. A main scanline (blue line N145° oriented) was performed along the scarp following the better exposure of the fracture and fault networks, as well as the main geothermal manifestations. Secondary scanlines/scan areas (from A to G; turquoise circles) were located along the main scanline (SL A, C, D, E) and the adjacent scarp (SL B and F, N80° oriented). b-c) Examples of fractures measured along scanline A (b), scanline E (c); d) example of fracture setting plain view (SL G), these few spots of pavements (5) were used for performing scan areas.

5. Results

5.1 Diffuse fluxes and soil temperature

Soil CO_2 fluxes ranged from 0.37 up to 2,927 g m^{-2} d^{-1}, with mean and median values of 197 g m^{-2} d^{-1} and 44.5 g m^{-2} d^{-1}, respectively, and standard deviation of ± 437 g m^{-2} d^{-1}. The cumulative frequency plot (Fig. 6a) of the CO_2 data shows two inflection points at LnϕCO_2 2.89 g m^{-2} d^{-1} (i.e., 18.1 g m^{-2} d^{-1}) and LnϕCO_2 5.65 g m^{-2} d^{-1} (i.e., 285.6 g m^{-2} d^{-1}). Population A represents 40% of the dataset with values ranging between 0.37 and 18.1 g m^{-2} d^{-1} with mean and median values of 5.0 g m^{-2} d^{-1} and 2.76 g m^{-2} d^{-1}, respectively, while the standard deviation is ± 5.04 g m^{-2} d^{-1}. Population B (43%) ranges from 21.4 and 285.6 g m^{-2} d^{-1}; the mean, the median, and the standard deviation are 95.7, 82.1 and ± 65.4 g m^{-2} d^{-1}, respectively. Finally, Population C includes 13% of the measurements and ranges from 390.3 and 2,926.7 g m^{-2} d^{-1}, with mean and median values of 874.8 g m^{-2} d^{-1} and 642.3 g m^{-2} d^{-1}. The standard deviation is ± 732.3 g m^{-2} d^{-1}.

Soil temperature data approximate a (Log)normal distribution, as highlighted by the cumulative frequency plot in Figure 6b. Values span over a wide range (from 24.8 up to 98.8 °C), with mean, median and standard deviation values of 46.4 °C, 42.2 °C, and ± 17.1 °C, respectively.

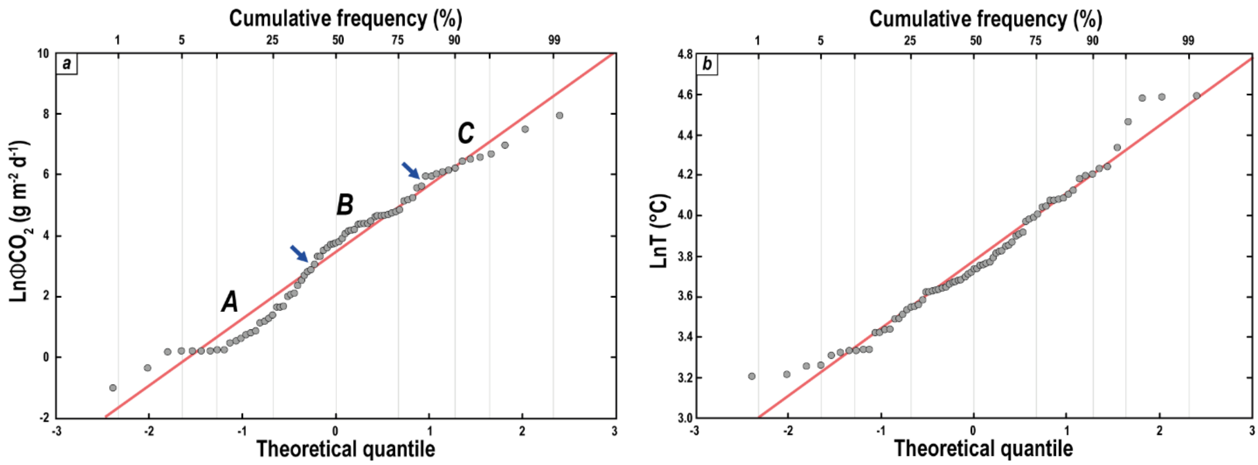

Figure 6. Cumulative frequency plots of the (a) soil CO_2 and (b) temperature measurements.

5.2 CO_2 output estimation

By applying the Sichel's t-estimator for the CO_2 output in the studied area, a value of 0.21 t d^{-1} was computed (with lower and upper confidence limits of 0.17 and 0.29 t d^{-1}, respectively), essentially due to population B (0.06 t d^{-1}) and C (0.15 t d^{-1}), being the contribution of population A (i.e., <0.001 t d^{-1}) negligible. The normalized total CO_2 flux from the soil (i.e., the total output divided by the area of the survey) was 155.5 t d^{-1} km^{-2}. The percentage contribution of each population constituting the whole dataset is reported in Table 1.

Table 1. *Percentage contribution of each population constituting the whole dataset used to estimate the total amount of $\phi CO2$ released from the study area.*

Variable	Surface area (m^2)	Population	Measurements (n.)	Total output (t d^{-1})	95% Confidence interval (t d^{-1})

ϕCO_2	1350	A	30	<0.001	-
		B	32	0.06	0.05-0.08
		C	12	0.15	0.12-0.21
		Outlier	1	<0.001	-
		Total	*75*	*0.21*	*0.17-0.29*

5.3 Distribution maps

The soil CO_2 flux and temperature distribution maps obtained by the kriging interpolation method are reported in Figure 7 (interpolation grid 1 x 1 m). The combination of three basic structures (2 Spherical plus Nugget effect) is the best model to describe the spatial variability of ϕCO_2 whereas the soil temperature spatial variability is best described by one spherical variogram. Variograms, variograms parameters, cross-validations of the mathematical model describing the experimental variogram of each map, standard deviation maps, and the measured values, are reported in the Supplementary Material.

CO_2 flux and temperature show a moderate visual correlation, with the upper values of both parameters located in the northern, central, and southwestern sectors of the study area whilst the lowest ones are mostly occurring in the easternmost zone (Fig. 7). In general, the highest CO_2 fluxes (up to 2927 g m^{-2} d^{-1}) and temperatures (up to 98.8 °C) were found in the central portion of the NW-oriented scarp that crosscuts the area, where the main structural lineaments were recognized.

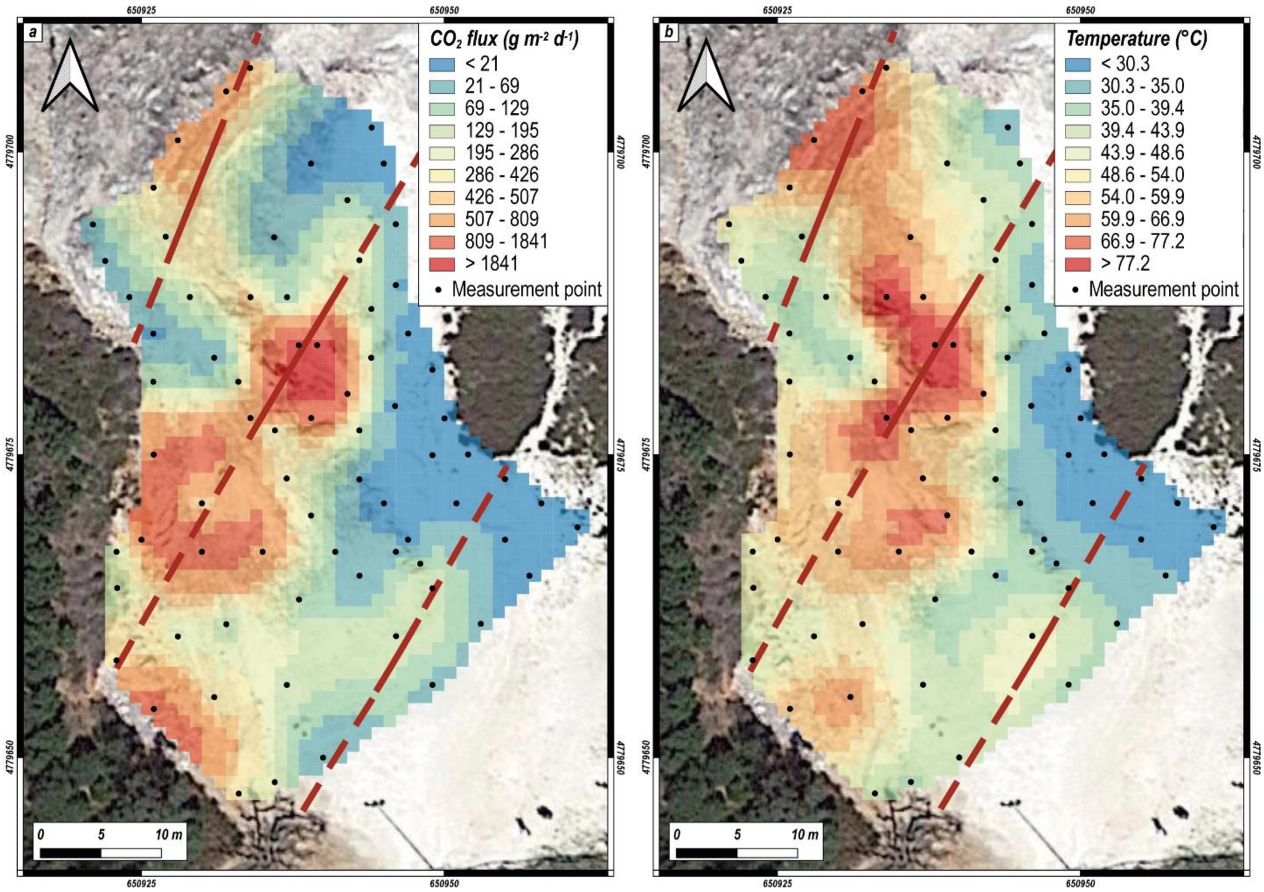

Figure 7. a) Soil CO_2 flux, and b) temperature distribution maps. Faults are reported as red lines.

5.4 Structural setting, fracture, and permeability analysis

A NNE-striking fault zone (the MMSP) crosses the study area (Figs. 1 and 2). This structure is at least 5 km long (Figs. 2 and 3) and is part of the NNE-trending fault system defining the transfer zone affecting the Larderello geothermal area (Liotta and Brogi, 2020). In the southern part, MMSP bounds the Neogene sediments filling the Lago Basin, whereas in the northern part it defines a splay of a NE-striking fault passing through the Larderello and Montecerboli villages (Fig. 2). In the area between Monterotondo Marittimo and Sasso Pisano, the fault zone consists of several subparallel and/or anastomosed NNE- and N-S-striking fault segments, dissecting the Jurassic-Tertiary succession of the Tuscan Nappe (Fig. 2). Steam and CO_2 emissions, hydrothermal alteration and silicization phenomena characterize the damage volumes of those fault segments affecting the Jurassic radiolarite (Diaspri Fm) (Fig. 8a) and the early Cretaceous limestone (Maiolica Fm). The geothermal manifestations mainly occur along an area between Monterotondo Marittimo and Sasso Pisano (Figs. 2, 3, and 4), thus indicating the trend of the main fault zone. This fault zone was the object of geothermal exploration during the past decades (Lazzarotto, 1967; Lazzarotto and Mazzanti, 1978; Minissale, 1991; Batini et al., 2003; Bertini et al., 2006; Romagnoli et al., 2010) and today, is still producing the steam feeding the power plants (www.arpat.toscana.it).

At the map scale, the main fault zone involves the Tuscan Nappe and separates the hanging wall, made up of the late Oligocene-early Miocene quartz-feldspar micaceous sandstone (Macigno Fm) with its basal Cretaceous-Oligocene shaly succession (Scaglia Toscana Fm), from footwall consisting of the basal carbonate-siliceous succession (Fig. 2). This latter fault block comprises two main Tuscan Nappe sub-units doubled during the collisional event of the Northern Apennines. The lower one is characterized by an exposed succession encompassed between the late Triassic evaporite (Burano Fm) and the late Oligocene-early Miocene quartz-feldspar sandstone and shale (Macigno Fm); this succession exhibits a significant tectonic omission resulting in the direct superimposition of the Macigno Fm on the early Jurassic massive limestone (Calcare Massiccio Fm) (Fig. 2b). The upper sub-unit is represented by a few klippen formed by a succession comprised between the Calcare Massiccio Fm and the Macigno Fm (Fig. 2b). The geological bodies belonging to the Sub-Ligurian and Ligurian domains (ophiolite, shale with interbedded limestone, marly limestone and quartz-sandstone) directly overlie the Tuscan Nappe sub-units, thus implying a robust tectonic omission having affected the original stacked units.

The main fault zone is well exposed in a sector of the *Le Biancane* natural park in the wall of abandoned quarries (Figs. 4a and 8b). The tens meters-thick fault zone consists of sub-vertical secondary faults striking N20-30° (Fig. 8b-e), clearly associated with the visible emission of vapors. The protolith is composed by the Jurassic siliceous beds (Fig. 8a). This succession is mainly characterized by thin (average 4-15 cm), whitish to brownish stratified chert beds rhythmically interbedded with shaly levels up to 1 cm thick. Some chert beds are pure and vitreous, while others are consisting of radiolarian (packstone to grainstone) chert, often laminated at the base of the strata. This succession is overlain by about 10 m of slightly calcareous radiolarian chert beds, thinly bedded (average 4-6 cm), highly siliceous passing to whitish to reddish limestones interbedded with shaly levels about 0.5-1 cm thick. Cherty beds are intensely fractured (up to 5-6 fractures per 10 cm), although these fractures are confined within the cherty beds without cutting the shaly levels separating the different siliceous beds (Fig. 8).

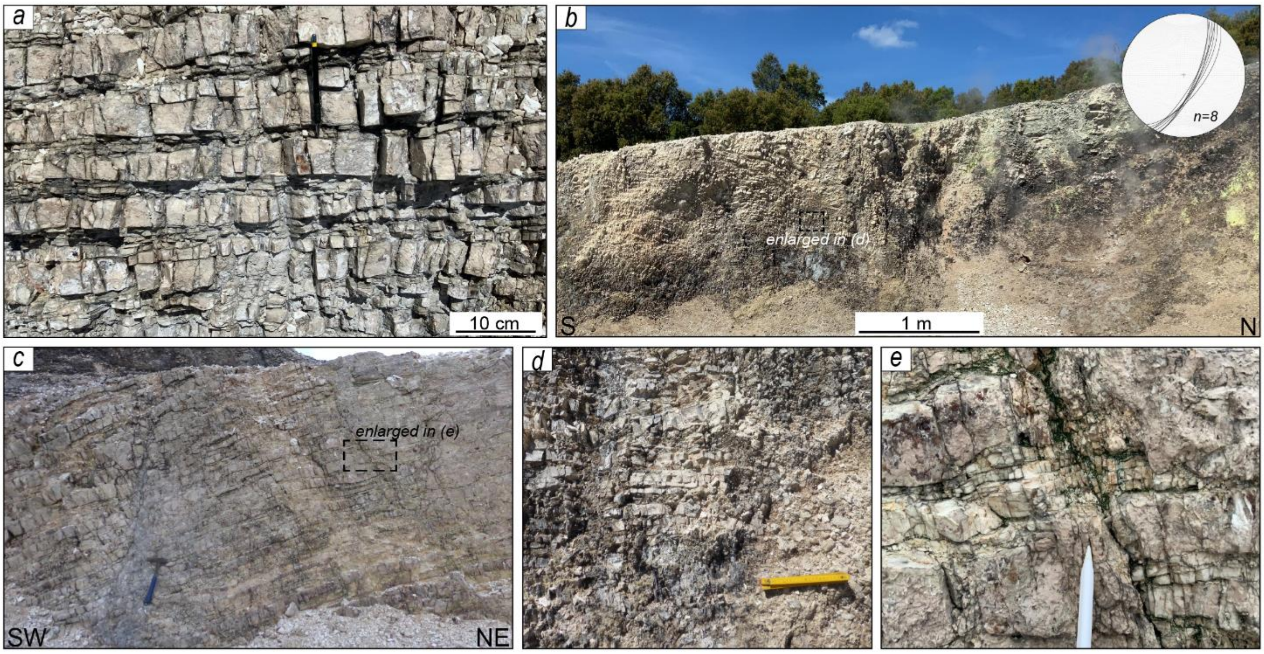

Figure 8. a) Photograph of the Jurassic siliceous beds (Diaspri Fm) exposed in the study area; b) panoramic view of the main fault zone exposed along the scarp (Fig. 5a); c) panoramic view of a minor fault exposed in the study area; d) detail of the fault zone showing highly fractured and altered (dark zones) Diaspri Fm due to the intense hydrothermal activity occurring along the fault zone; e) detail of the shale and siliceous beds cut by a minor fault.

The fractures were classified in families for modeling purposes. The grouping was based on the orientation and type of fractures (joints, faults) (Fig. 9). For the DFN modeling, the current fracture orientation was used for each scanline (Fig. 9c). We have considered fractures likely predating, or coevally formed during tilting of beds, as the ones clustering in stereonets after applying the bed restoration (normal to bedding), whereas fractures formed after the tilting, clustered better on the current orientation. From the fracture analysis seven families were differentiated (Table 2). Most fractures (Sets 1 - 4) are stratabound and, according to field observations, can be classified as joints. Sets 1 and 2 are characterized by lower clustering (K < 70), in contraposition to the Sets 3 and 4 which have a more regular orientation (K = 125-126). By considering their orientation and field observations, Set 5 seems to be strictly fault related, while Sets 6 and 7 correspond to incipient faults. In terms of fracture density, some families of fractures (Sets 5 and 6) are more abundant towards the fault slip surfaces (or strictly located in their vicinity), while other families seem to be more unevenly distributed.

Table 2. *Main fracture families differentiated from the scanlines.*

Set	Type	Orientation				Notes
		Dip direction (°)	*Strike (°)*	*Mean dip (°)*	*Fisher (K)*	
1	Joint	167	77	84	39	After rotation
2	Joint	107	17	80	65	After rotation
3	Joint	245	155	85	125	After rotation
4	Joint	204	114	87	126	After rotation
5	Fault related Joint	127	37	69	103	Without rotation
6*	Shear joints/Fault	120	30	85	200**	Without rotation
7*	Shear joints/Fault	220	130	85	200**	Without rotation

Notes: Set 6* represents fault-parallel, non-stratabound fractures strictly located in the proximity of the fault surface. ** K value was assumed due to low data density.

The apertures of the fractures range from 0.05 mm to 0.1 mm, which agree with the narrow beds (generally <20 cm). The other geometric features are summarized in Table 3. The fracture linear intensity (*P10*) is relatively high and tends to increase towards the main fault surface located to the North of the model, consistent with the field observations (Fig. 9b). Some variability in this trend is related to the presence of secondary fault structures, whereas zones with undetected fractures are related to cementation and alteration. The secondary fault structures show cm- to few meters displacements.

Table 3. *Fractures geometric attributes used for DFN models construction.*

Set	Length (cm)				Aspect ratio	Fracture intensity		
	Min	*Max*	*Mean*	*St. Dev.*		*P10* Mean	*P10* St. Dev.	*P32*/*P10*
1	5	20	10.0	3	1.4	24.4	3.3	1.1
2	5	20	10.0	3	1.4	25.1	18.4	1.1
3	5	15	7.0	2	1.0	9.8	3.3	0.8
4	5	15	7.0	2	1.0	7.4	3.6	0.8
5	3	10	5.0	2	0.7	8.6	7.8	0.6
6*	-	-	600	-	2.0	5.0	-	1.0
7*	-	-	250	-	2.0	1.0	-	1.0

Notes: the aspect ratio is provided for an average bed thickness of 7 cm. The geometrical properties of the set 6 and 7 are estimated since are out of scale at the outcrop.

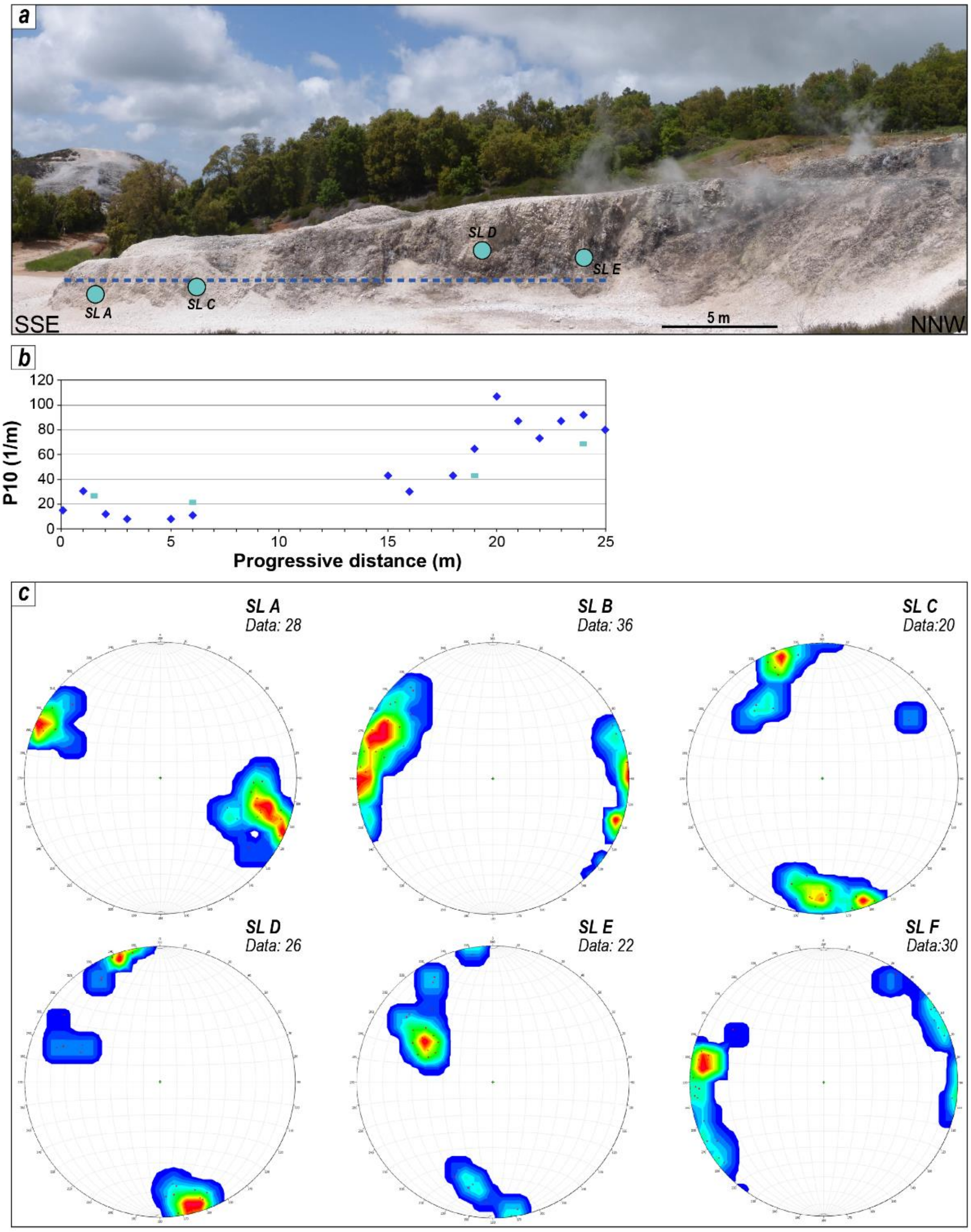

Figure 9. a) Panoramic view of the scarp where the main scanline (dashed blue line) and the secondary scanlines (SL A, SL C, SL D, SL E) were performed; b) linear fracture intensity *P*10 along the main scanline indicated in (a); c) stereoplots of the fractures (poles of planes) measured in each of the indicated Scanline.

During the DFN modeling, a total of 100 realizations were performed to ensure the significance of the calculated values, obtaining coefficient values of variation below 0.1, indicating stables and representative volumes (Zhang et al., 2000). The upscaled hydraulic properties (porosity and permeability) follow the same trend provided by the linear fracture intensity in Figure 9b. For a better comprehension, the model was divided into four sectors based on the results and the field observations (Table 4). Sectors I and III are moderate to highly fractured areas (*P32* in the range of 50-100 m^2/m^3) characterized by the presence of sporadic subsidiary faults. Fracture porosity is below 1%, the modeled horizontal component of the permeability is in the order of 10^{-15} m^2 while the vertical one is near 10^{-16} m^2. Sector II is poorly affected by fractures, and therefore the values of fracture porosity and permeability are very low and likely negligible. The Sector IV corresponds to the area with the highest geothermal emissions, and it is characterized by a relatively larger fracture density (*P32* > 100 m^2/m^3). Most of these additional fractures corresponds to the Set 6 (N30° striking; Table 3), which is extremely localized and persistent. In this regard, the model indicates a mild increment of one order of magnitude for the horizontal component and three orders of magnitude for the vertical component of the permeability tensor.

Table 4. *Summary of the modelled fracture properties.*

Sector	**Φ_f [%]**		**k_{xx} [10^{-15} m^2]**		**k_{yy} [10^{-15} m^2]**		**k_{zz} [10^{-15} m^2]**		***P32* [m^2/ m^3]**	
I (0-6m)	0.64	±0.09	61	±12	44	±22	0.1	-	63.66	±8.93
II (7-13m)	0.03	±0.01	3.0	±1.3	3.6	±2.0	0.1	-	2.95	±1.14
III (14-20m)	0.82	±0.29	85	±24	67	±32	0.74	1.9	82.00	±29.0
IV (>20m)	1.10	±0.09	130	±22	180	±50	19	32	110.42	±9.38

Notes: The distances reported in the column sectors, refers to the fig. 9b. Reported error corresponds to the standard deviation. Φ_f is the fracture porosity, k_{xx} is the permeability component N30°-oriented, k_{yy} is the permeability component N120°-oriented, k_{zz} is the vertical permeability component.

6. Discussion

6.1 Origin and transport of soil CO_2 degassing

The cumulative frequency plot (Fig. 6) has allowed identifying the presence of different populations of CO_2 fluxes, suggesting three distinct sources or transport mechanisms of carbon dioxide characterized by threshold and mean values of the same order of magnitude as those recognized by Cabassi et al. (2021) in the southern part of the *Le Biancane* natural park (Fig. 3). The low-flux population (A) shows mean and upper threshold values of ~5 and ~18 g m^{-2} d^{-1}, respectively, and indicates a biological source (i.e., plant and microbial respiration and organic decomposition; Raich and Schlesinger, 1992; Cardellini et al., 2003; Chiodini et al., 2008; Viveiros et al., 2010, 2020). Population C is likely related to a hydrothermal source, being the CO_2 values >390 g m^{-2} d^{-1} (e.g., Viveiros et al., 2010, 2020). Consequently, population B can be linked to mixing processes, to different degrees, between populations A and C. However, when the CO_2 flux and the corresponding $\delta^{13}C$-CO_2 data of Venturi et al. (2019), collected 100 m far from the study area of the present work, are plotted against each other (Fig. 10) the lowest fluxes (<~20 g m^{-2} d^{-1}) show wide variability in terms of carbon isotopes, from -16.1‰ up to -0.53‰, the latter being much heavier than a purely biogenic CO_2 (e.g., Sharp, 2017). This relatively large isotopic interval can be due to different fractionation processes such as mixing between biogenic (e.g., −33 to −23‰ for C3 plants; Sharp,

2017) and hydrothermal (e.g., the Larderello geothermal reservoir; Gherardi et al., 2005) sources, diffusive transport (Federico et al., 2010), and microbial consumption at shallow depths (Venturi et al., 2019) or methanogenic processes occurring in the hydrothermal reducing environment (Whiticar, 1999). Biological CO_2 uptake and fixation processes are indeed expected to produce a ^{13}C-rich residual CO_2 in interstitial soil gases and are the likely responsible for the heavier $\delta^{13}C$-CO_2 values measured at Monterotondo (Venturi et al., 2019 and references therein). Regardless of the origin of CO_2, fluxes >~20 g m^{-2} d^{-1} show a clear hydrothermal isotopic signature. However, when ϕCO_2 values comprised between ~20 and ~300 g m^{-2} d^{-1} are considered, the carbon isotopes reach significantly high values (up to +3.41‰). These strikingly positive values are likely associated with a two-stage fractionation process due to boiling during fluid ascent within the reservoir and a subsequent isotopic enrichment as CO_2 diffuses through the soil (Rissmann et al., 2012). In this way, fluxes ranging between ~20 and ~300 g m^{-2} d^{-1} likely suggest that diffusive and advective transport processes may occur simultaneously. Fluxes higher than ~300 g m^{-2} d^{-1}, associated with soil temperature >53 °C, seem to be linked to a purely advective transport, although a microbial CO_2 uptake and fixation positive shift occur (Venturi et al., 2019; Fig. 10).

Based on the: i) proximity of our and Venturi et al. (2019) study areas, ii) tectonic setting and iii) hydrothermal evidence (Figs. 2 and 3), the CO_2 emissions from both sites can be assumed to be governed by the same geochemical processes. The ϕCO_2 intervals identified in Fig. 10 from Venturi et al. (2019) data (i.e., <20; 20-300; >300 g m^{-2} d^{-1}) well agree with those identified in the study area distinguishing the three populations of fluxes (Fig. 6). In this context, fluxes of population A (i.e., <18 g m^{-2} d^{-1}; Fig. 6) are likely linked to a purely diffusive transport driven by a concentration gradient, while population C data (>390 g m^{-2} d^{-1}; Fig. 6) are driven by an advective transport related to a pressure gradient. Soil CO_2 fluxes between 21 and 290 g m^{-2} d^{-1} (Population B; Fig. 6) can be regarded as representative of a combined diffusive–advective transport mechanism.

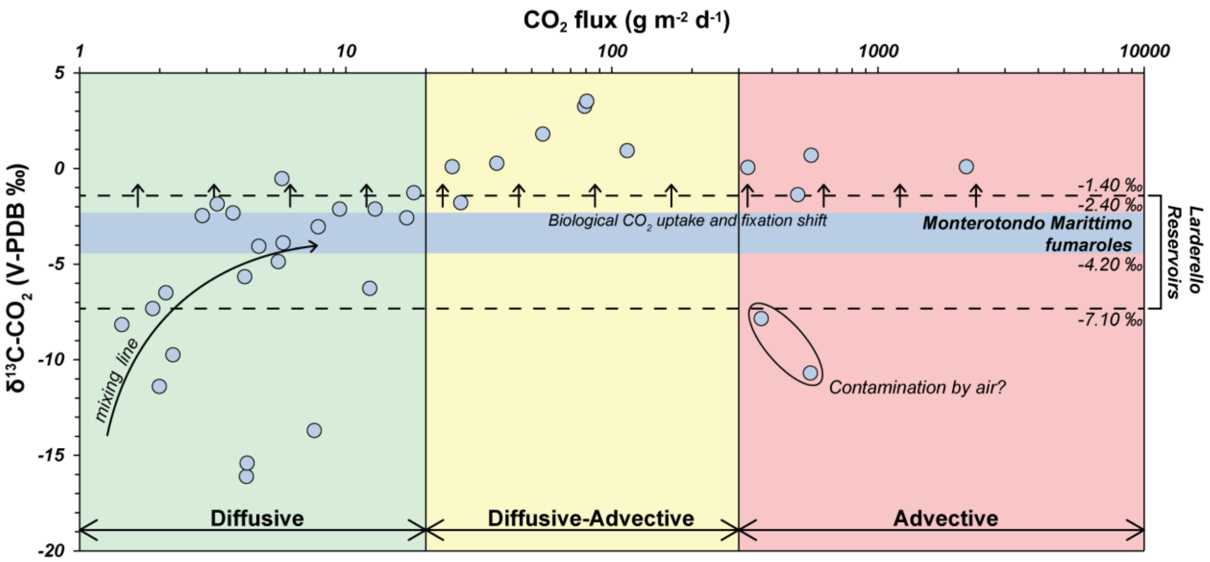

Figure 10. Soil CO_2 flux vs. isotopic composition of fluxes from the Monterotondo Marittimo area (data from Venturi et al., 2019). $\delta^{13}C$-CO_2 composition of Monterotondo Marittimo fumaroles (Venturi et al., 2019; Leila et al., 2021) and Larderello reservoirs are also reported (Gherardi et al., 2005).

6.2 Correlation between faults/fractures and fluid emissions

The exposed rocks are highly fractured as revealed by the significantly high values of *P*32. However, the rock volume likely contributing to the fluid transport corresponds to the highly fractured siliceous rock layers in the proximity of faults. On the other hand, far from the fault zones fractures do not (or rarely) affect the interbedded thin shale layers separating the siliceous beds and therefore these levels play the role of mechanical boundaries (Fig. 11a) and fluid transport buffer zones. Only a few fractures, most likely incipient fault planes, cut both the shaly and cherty beds. These features are mainly found near main fault slip surfaces and are responsible for localized vertical connectivity of the fracture network (Fig. 11b,c). The presence of subsidiary faults is illustrated by a complex fracture intensity distribution (Fig. 9b) along the main scanline that may locally affect the fluid storage and transport (e.g., Volatili et al. 2022).

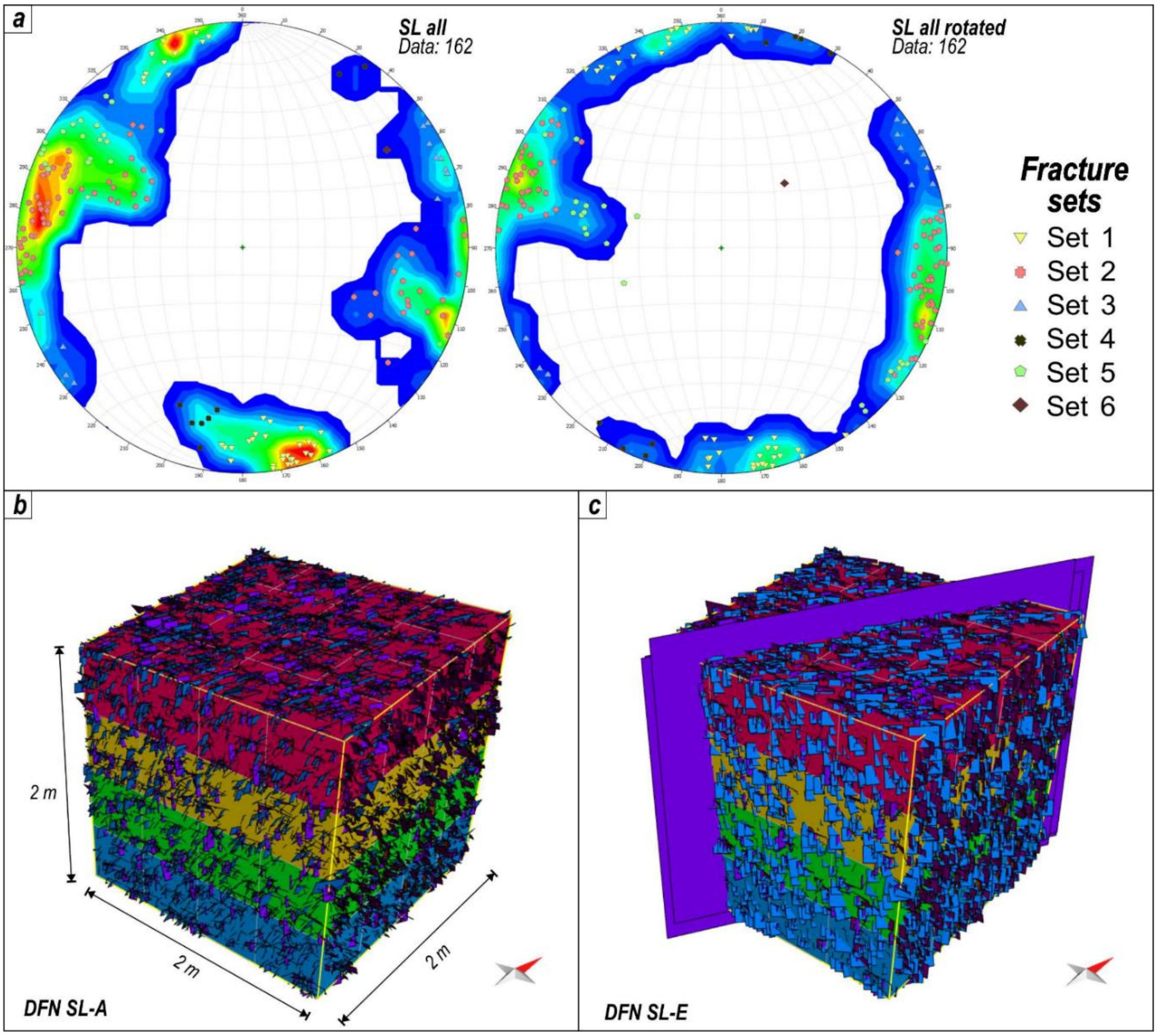

Figure 11. a) Stereonet data from all the scanlines with and without rotation; b) detail of the DFN models in proximity of the (b) scanlines SL A and (c) SL E. Most of the modelled fractures are stratabound, however near secondary faults non-stratabound fractures parallel to faults N30° striking are present (purple).

In terms of vertical pathways for CO_2, the main conduits are represented by the localized pervasive fault-related fractures (i.e., Set 6). Actually, the highest CO_2 fluxes (i.e., >300 g m^{-2} d^{-1}), likely related to a pressure-gradient controlled transport (Fig. 10), were mainly measured in correspondence with the NE-SW faults (Fig. 12a) characterizing the MMSP area (Figs. 2 and 3) which is part of the Larderello transfer fault system (Liotta and Brogi, 2020) (Fig. 1). This transfer fault system shows a compartmentalized permeability whose maximum is in the tract comprised between Monterotondo Marittimo and Sasso Pisano, as indicated by the geothermal manifestations only occurring in this section (Figs. 3 and 4). Nevertheless, although these manifestations characterize the whole fault zone between Monterotondo Marittimo and Sasso Pisano localities, the maximum CO_2 fluxes are mainly concentrated in the *Le Biancane* area (Venturi et al., 2019; Leila et al., 2021; Cabassi et al., 2021) (Figs. 3 and 7). Based on our dataset, this can be explained by the enhanced fracture permeability induced by the numerous fault segments (Figs. 2 and 3) which consist of anastomosed structures defining the first-order transfer fault zone (Fig. 2). While fault-related fractures enhance the vertical permeability along the fault strike, the diffuse stratabound fractures permit the CO_2 to migrate laterally. This migration is facilitated by a significant permeability anisotropy characterized by horizontal components (k_{xx} and k_{yy}) up to three orders of magnitude higher than the vertical component (k_{zz}). This explains why the geothermal manifestations are widespread in a large area around the fault zone, even distant from the fault-related fractures. According to the CO_2 flux and temperature distribution, a moderate positive correlation between the two parameters in both the whole analyzed area (Figs. 7 and 12b) and along the NW-striking transect that cross-cut the fault zone (Fig. 12c) is observed.

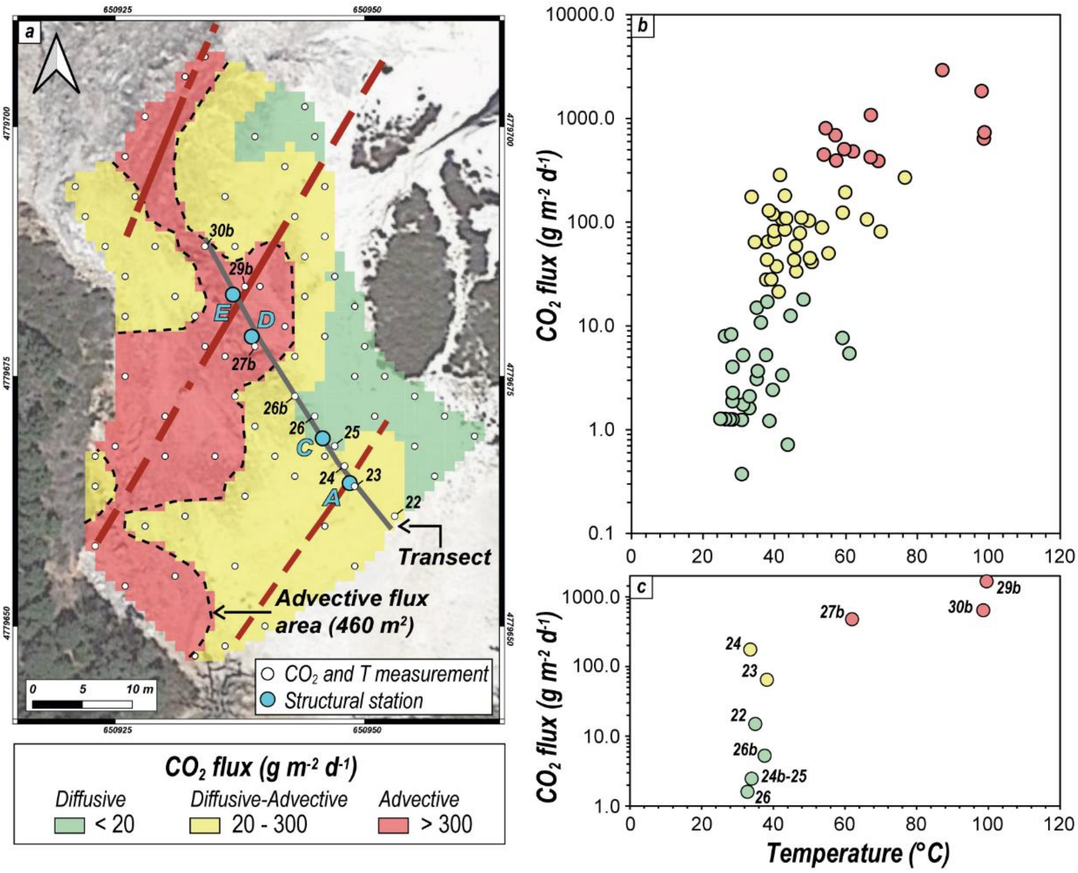

Figure 12. a) Distribution map of the soil CO_2 flux divided by the inferred transport mechanisms; b) relationship between soil CO_2 and temperature in the study area and c) along the transect in (a).

Numbers in (a) and (c) represent the id of the measurement points reported in the supplementary material.

The correlation among the CO_2 fluxes and soil temperatures (both measured in the field and derived from the kriging intepolation) recorded along and near (± 3 m) the transect represented in Figure 12a, and the results of the DFN modeling (porosity, *P32* and permeability tensor) is here evaluated by using scatter plots (Fig. 13).

Results indicate a good control of the *P32* and porosity on the distribution of both CO_2 fluxes and soil temperatures following power laws with regression coefficients 0.66 and 0.78, respectively. In general, a clear positive correlation was found for the permeability components (R^2 >0.8) and the soil temperature. The scatter plots between CO_2 fluxes and permeability seems to indicate two different populations depending on if the area is affected or not by persistent fractures. In fact, any attempt to find a correlation between these parameters without separating both populations does not indicate a correlation (R^2 < 0.5). After removing the points with high permeability (associated with the persistent fractures), a regression coefficient higher than 0.7 was obtained. Correlations of both CO_2 fluxes and soil temperatures with the vertical component of the permeability is unclear due to the high control of the low-permeability shaly layers into the model.

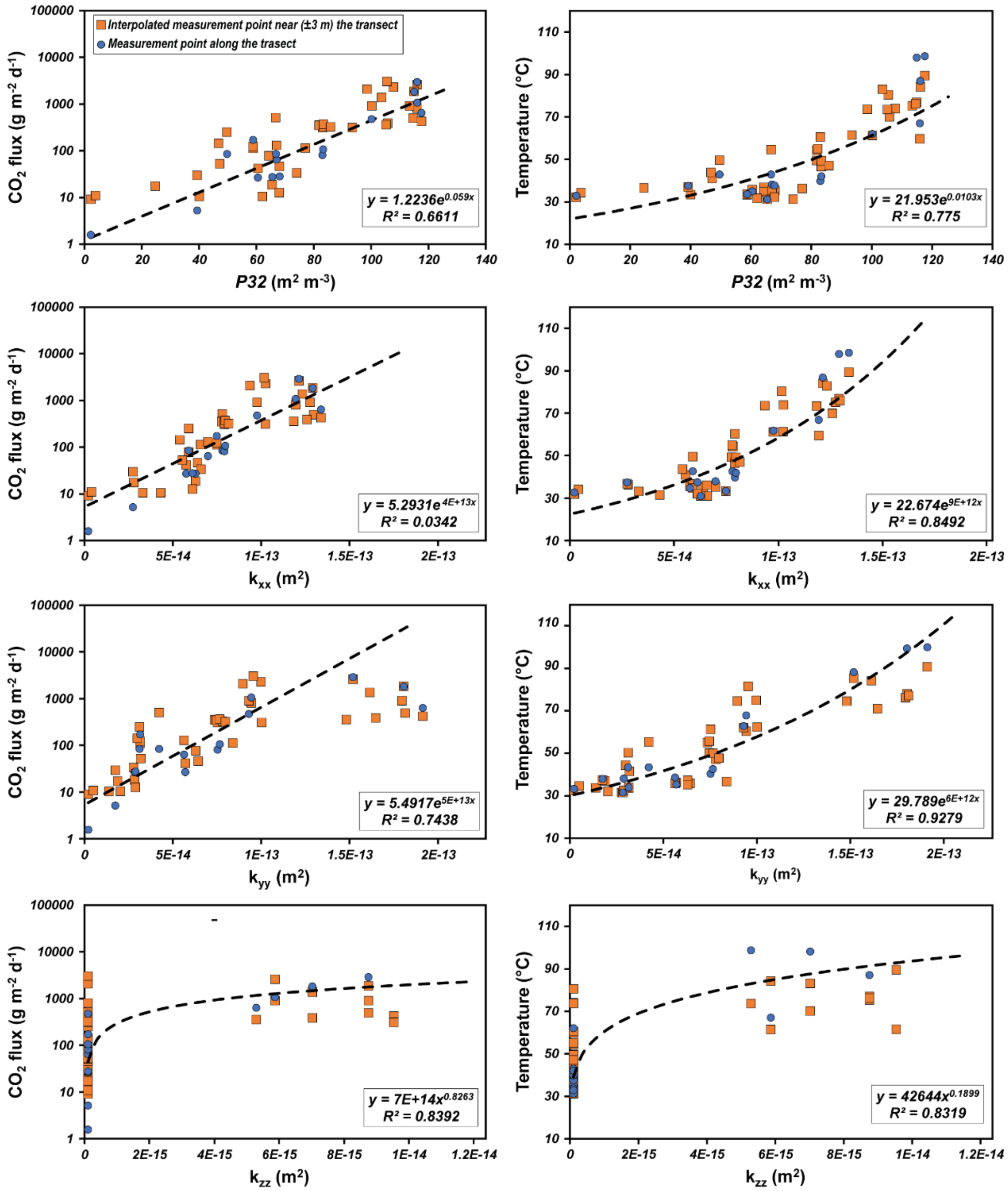

Figure 13. Correlation among soil CO_2 flux and temperature measurements (blue circles measured, orange squares interpolated) and the DFN modeling outputs (*P32*, k_{xx}, k_{yy}, k_{zz}).

Another way to note the correlation between geothermal soil degassing and fracture properties is noted by comparing the results of the DFN modeling along the same transect (Fig. 14), where CO_2 fluxes and soil temperatures are reported with *P*32 and horizontal permeability (k_{xx}) values. CO_2 fluxes and soil temperature behave similarly where the highest values of both parameters are found. In fact, in the north-western portion of the transect, in the proximity of the scanlines D and E (Fig. 5 and 12a), fluxes higher than 480 g m^{-2} d^{-1} are associated with soil temperatures >62 °C (and maximum up to 98.6 °C) (Figs. 12c and 14). Such emissions are linked to the enhanced fracture permeability within the fault damage zone (Sector IV; Table 4), characterized by *P*32 higher than 100 m^2/m^3, and permeability values of 10^{-14} m^2 and 10^{-13} m^2, for the vertical and horizontal component, respectively (Figs. 13 and 14). The presence of sub-vertical, persistent slip surfaces and related damage zones striking N20-30° (Figs. 8, 11) would enhance the efficient advective ascent of high amounts of CO_2 and heat to the surface, driven by a pressure gradient (Fig. 10). The rapid rise of the gases would prevent the fractionation of the CO_2 isotopologues, thus maintaining the isotopic signature of the CO_2 source of the reservoir (Fig. 10) and favoring the rise of steam without appreciable condensation (Capasso et al., 2001; Camarda et al., 2007; Rissmann et al., 2012). This results in a high CO_2 emission and a sensible temperature anomaly at the surface, indicative of active hydrothermal circulation of geothermal fluids along deep-rooted fractures (Giammanco et al., 2016; Rolleau et al., 2017; Lamberti et al., 2019; Taussi et al., 2021).

Moving toward the central part of the transect (Fig. 14), near the scanline C (Fig. 5 and 12a), different structural features characterize the protolith. *P*32 and permeability values drop down to 2-4 m^2/m^3 and 10^{-15} m^2, respectively (Fig. 13 and 14; Sector II; Table 4). At the same time, the measured CO_2 fluxes dramatically decrease down to <6 g m^{-2} d^{-1}, while soil temperatures are relatively constant (between 32.9 and 37.6 °C). The protolith is here affected by intense cementation and alteration, and it is characterized by low persistent fracturing only limited to the siliceous beds without cutting the interlayered shale (Fig. 8). In this case, the low-permeability favors the slow and concentration-driven movement of the CO_2, therefore, boosting the fractionation processes (Fig. 10; Camarda et al., 2007) at a medium-low temperature (i.e., slightly higher than the atmospheric one during the fieldwork).

A decoupling between CO_2 and temperature is observed in the south-western part of the transect (Figs. 12a and 14), far from the main slip surfaces. Here, the CO_2 fluxes are between 65 and 175 g m^{-2} d^{-1} while temperatures remain constant at about 34-38 °C. Near scanline A (Fig. 5 and 12a) – except for measurement #24 where an incipient fault is nearly located – fracture network is characterized by relatively moderated volumetric fracture intensity (*P*32) ranging between 60 and 80 m^2/m^3, and permeability values in the order of 10^{-14} and 10^{-16} m^2 for the horizontal and vertical components, respectively (Fig. 13; Sector I; Table 4). This fracture setting permits a diffuse degassing, but the inadequate pressure of the geothermal fluids triggers the vapor condensation. A loss of heat, thus, occurs on the rising way through the not well-developed fractures (Giammanco et al., 2016) together with the dispersion of the ascending gas over larger areas – with consequent fractionation processes (Fig. 10) – taking advantage of the higher ground permeability (Fig. 13).

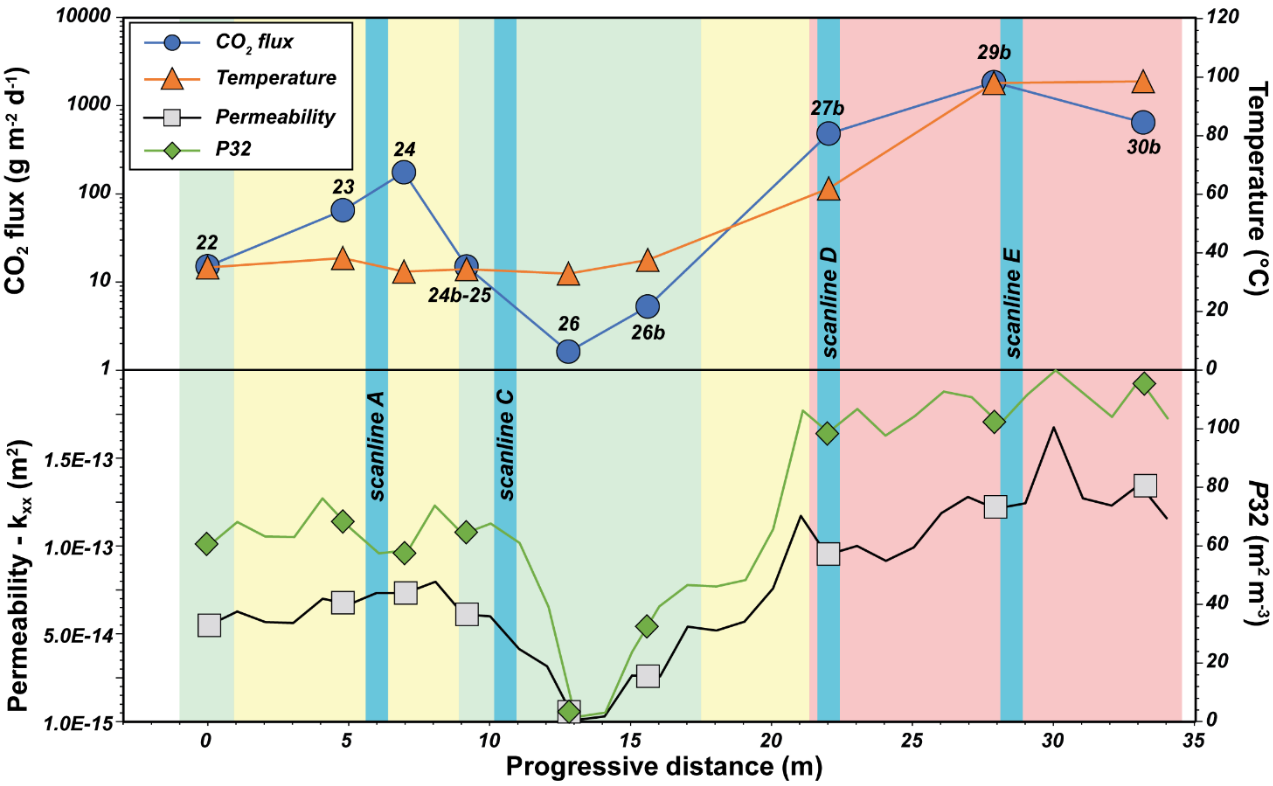

Figure 14. Soil CO_2 flux, temperature, *P*32 and permeability measurements carried out along the transect represented in Figure 12, which runs orthogonally to the MMSP fault zone. The location of the secondary scanlines is also shown in turquoise. Background colors represent the main transport mechanism of CO_2; green: diffusive, yellow: mixed diffusive and advective, red: advective.

The structural setting has also implications for the quantity of CO_2 emitted from the investigated fault zone. The normalized CO_2 output from the whole studied area (1,350 m^2) was estimated at ~155 t d^{-1} km^{-2}, virtually equal to that computed by Cabassi et al. (2021). This value is much higher than the endogenous emission at e.g. Los Humeros (Mexico; ~52 t d^{-1} km^{-2}; Jentsch et al., 2020), Rotorua (New Zealand; 40-70 t d^{-1} km^{-2}; Werner and Cardellini, 2006) or Reykjanes (Iceland; ~53 t d^{-1} km^{-2}; Fridriksson et al., 2006), and on the same order of magnitude of e.g. Ischia and Latera (Italy; ~173 and ~112 t d^{-1} km^{-2}; Chiodini et al., 2004; Chiodini et al., 2007), Furnas (Azores; up to ~112 t d^{-1} km^{-2}; Viveiros et al., 2020) and Copahue (Chile-Argentina; ~175 t d^{-1} km^{-2}; Chiodini et al., 2015). However, most of the CO_2 discharge is related to the highest fluxes pertaining to the hydrothermal population (C; Table 1) – estimated in 0.15 t d^{-1} – which are focused in a restricted area of about 460 m^2 (Fig. 12), in correspondence with the NE-SW fault, confirming the pivotal role of the structural characters in the control of the fluid emissions.

7. Conclusions

The Monterotondo Marittimo-Sasso Pisano area stands at the border of a pull-apart structure (Lago Basin), developed within a regional active transfer zone characterizing the Larderello geothermal field (Liotta and Brogi, 2020). This structure acts as a preferential way for mantle-derived fluids ascent and permits the geothermal fluids to be conveyed from the reservoir(s) to the shallower levels

(Fig. 15a). The integration between CO_2 flux measurements and fracture distribution, crossing a sector of the transfer zone, indicates that fracture-induced permeability is the main factor in controlling the CO_2 local emission. A quantification of this implies permeability values in the order of 10^{-14} m^2 to permit degassing. Small variations of this value influence the transport mechanism of CO_2, which can pass from diffusive to advective through the mixing of both processes (Fig. 15b). The diffusive transport mechanism is driven by a concentration gradient and characterizes those areas usually located far from the main shear zone (Fig. 15b,c), where fractures have a low persistence and are mainly limited to the stratabounds, thus indicating that the lateral migration of CO_2 is driven by layering (Fig. 15b,c). Differently, CO_2 advective transport is favored in the fault damage zone, where pervasive fractures that directly affect the reservoir (Fig. 15a) allow the rapid rise of high amounts of CO_2 and steam (Fig. 15b,c), avoiding $\delta^{13}C$-CO_2 fractionation of soil gas and maintain high temperatures. A combination of the diffusive and advective types of transport occurs in those transitional areas – or near the incipient faults (Fig. 15b) – where the influence of the main shear zone is still present. Here, fractures characterized by moderate persistence and intermediate permeabilities ensure a high degassing (Fig. 15b,c), but they do not prevent the vapor from condensation and heat loss. Finally, considering the regional setting, our results enforce the view that the transfer zones are favorable regional structures to localize the circulation of fluids, enhancing significant vertical permeability.

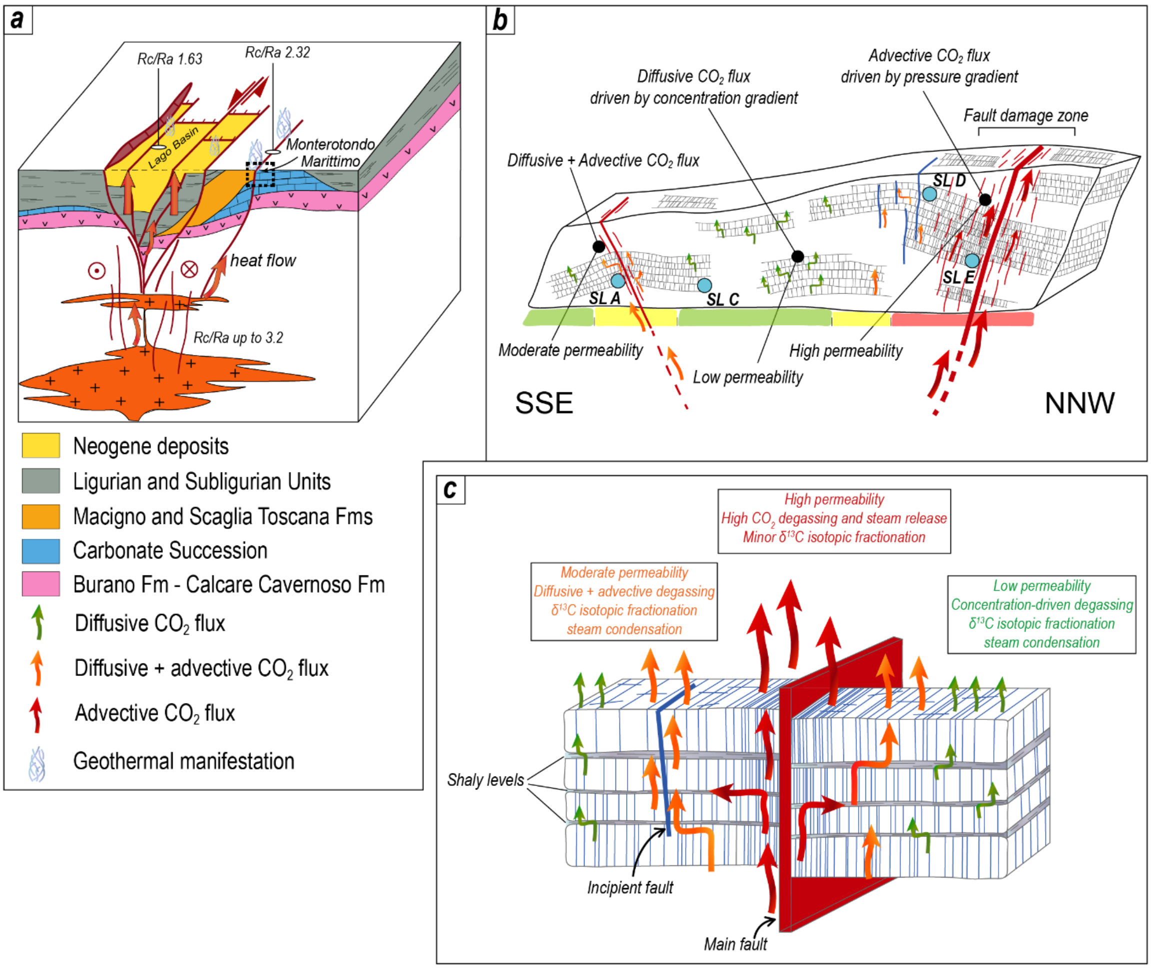

700

Figure 15. a) Geological sketch (not to scale) illustrating the tectonic and geothermal context of the Monterotondo-Sasso Pisano area, in the frame of the Lago pull-apart Basin developed within the transfer zone affecting the geothermal area of Larderello; b-c) local (b) and conceptual (c) models of the behavior of the CO_2 and steam emissions and transport mechanism, influenced by the enhanced permeability through the fault zone.

Acknowledgements

This research is framed in the cooperation with the UNESCO Tuscan Mining Geopark (https://parcocollinemetallifere.it/). Alessandra Casini, Elena Buracchi, Giancarlo Pagani are strongly thanked for motivating this research and for the continuous exchange of geological information. This work was partially financially supported by the laboratory of Stable Isotope Geochemistry of the Department of Earth Sciences and CNR-IGG of Florence. A.B., D.L., and M.Zu. received funding from the European Community's Seventh Framework Programme under grant agreement No. 608553 (Project IMAGE). M.Zu. received funding also from the Italian Ministry of University and Research (MIUR), through the program PON-AIM (Attraction and International Mobility) – project no. 1815472, Activity 1, line 1. The 3D fracture modeling was performed using Move^{TM} educational licenses provided by Petroleum Expert Limited (PETEX) to the Department of Earth and Geoenvironmental Sciences of the University of Bari (contact L. Spalluto) and the Geology Division of the University of Camerino (contact M. Zambrano). M.T. is grateful to University of Urbino for funds received through a post-doc grant. Data from the Alessio Cerboneschi's master thesis have been used for reproducing part of the geological map of Figure 2. Gabriele Boschi is kindly acknowledged for his help during the sampling campaigns. This manuscript largely benefitted of the detailed, useful, and insightful comments of an anonymous reviewer, which is sincerely thanked. Chris Bromley is also acknowledged for editorial handling.

References

Agosta, F., Alessandroni, M., Antonellini, M., Tondi, E., 2010. From fractures to flow: a field-based analysis of an outcropping carbonate reservoir. Tectonophysics, 490, 197-213.

Agostinetti, N.P., Licciardi, A., Piccinini, D., Mazzarini, F., Musumeci, G., Saccorotti, G., Chiarabba, C., 2017. Discovering geothermal supercritical fuids: a new frontier for seismic exploration. Scientific Reports 7, 14592.

Anderson, T.R., Fairley, J.P., 2008. Relating permeability to the structural setting of a fault-controlled hydrothermal system in southeast Oregon, USA. Journal of Geophysical Research, 113, B05402.

Antonellini, M., Cilona, A., Tondi, E., Zambrano, M., Agosta F., 2014. Fluid flow numerical experiments of faulted porous carbonates, Northwest Sicily (Italy). Marine and Petroleum Geology, 55, 186-201.

Baldi, P., Bertini, G., Cameli, G.M., Decandia, F.A., Dini, I., Lazzarotto, A., Liotta, D., 1994. Tettonica distensiva post-collisionale nell'area geotermica di Larderello (Toscana meridionale). Studi Geologici Camerti 1, 183–193.

Barbier, E., 2002. Geothermal energy technology and current status: an overview. Renewable and Sustainable Energy Reviews 6, 3-65.

Barcelona, H., Maffucci, R., Yagupsky, D., Senger, M., Bigi., S., 2020. Discrete fracture network model of the vapor zone leakages at the Copahue geothermal field. Journal of Structural Geology 140, 104155.

Barchi, M.R., 2010. The neogene-quaternary evolution of the Northern Apennines: crustal structure, style of deformation and seismicity. In: In: Beltrando, M., Peccerillo, A., Mattei, M., Conticelli, S., Doglioni, C. (Eds.), The Neogene-Quaternary Evolution of the Northern Apennines: Crustal Structure, Style of Deformation, Seismicity 36 Journ. Virt. Explorer.

Bartole, R., 1995. The North Tyrrhenian-Northern Apennines post-collisional system: constraints for a geodynamic model. Terra. Nova 7, 7–30.

Barton, N.R., Choubey, V., 1977. The shear strength of rock joints in theory and practice. Rock Mechanics, 10 (1-2), 1-54.

Barton, N., Bandis, S., Bakhtar, K., 1985. Strength, deformation and conductivity coupling of rock joints. International Journal of Rock Mechanics and Mining Sciences & Geomechanics Abstracts, Vol. 22 (3), 121-140.

Batini, F., Burgassi, P.D., Cameli, G.M., Nicolich, R., Squarci, P., 1978. Contribution to the study of the deep lithospheric profiles: deep reflecting horizons in Larderello-Travale geothermal field. Mem. Soc. Geol. It. 19, 477–484.

Batini, F., Brogi, A., Lazzarotto, A., Liotta, D., Pandeli, E., 2006. Geological features of Larderello-Travale and Mt. Amiata geothermal areas (southern Tuscany, Italy). Episodes 26, 239-244.

Bellani, S., Brogi, A., Lazzarotto, A., Liotta, D., Ranalli, G., 2004. Heat flow deep temperatures and extensional structures in the Larderello Geothermal Field (Italy): constraints on geothermal. J. Volc. Geoth. Res. 132, 15–29.

Bentivegna, M., 2010. Il Patrimonio Geologico: una risorsa da proteggere e valorizzare. Geologia dell’Ambiente. Periodico della SIGEA (Società Italiana di Geologia Ambientale). Supplemento al n.2/2011 ISSN 1591-5352. Atti del Convegno Nazionale, 29-30 April, 2010, Sasso di Castalda – Potenza (Italy). (In Italian)

Bertani, R., Thain, I., 2002. Geothermal power generating plant CO_2 emission survey. IGA News, 49, pp. 1-3.

Bertini, G., Cameli, G.M., Costantini, A., Decandia, F.A., Di Filippo, M., Dini, I., Elter, F.M., Lazzarotto, A., Liotta, D., Pandeli, E., Sandrelli, F., Toro, B., 1991. Struttura geologica fra i monti di Campiglia e Rapolano Terme (Toscana meridionale): stato attuale delle conoscenze e problematiche. Studi Geol. Camerti Spec. 1, 155–178.

Bertini, G., Casini, M., Gianelli, G., Pandeli, E., 2006. Geological structure of a long-living geothermal system, Larderello. Italy. Terra Nova 18, 163–169.

Bianco, C., Godard, G., Halton, A., Brogi, A., Liotta, D., Caggianelli, A., 2019. The lawsonite-glaucophane blueschists of Elba Island (Italy). Lithos 348–349, 105198.

Billi, A., Salvini, F., Storti, F., 2003. The damage zone-fault core transition in carbonate rocks: implication for fault growth, structure and permeability. Journal of Structural Geology, 25, 1779-1794.

Bonnet, E., Bour, O., Odling, N. E., Davy, P., Main, I., Cowie, P., Berkowitz, B., 2001. Scaling of fracture systems in geological media. Reviews of geophysics, 39(3), 347-383.

Brogi, A., 2004. Miocene low-angle detachments and upper crust megaboudinage in the Mt. Amiata geothermal area (Northern Apennines, Italy). Geodin. Acta 17, 375–387.

Brogi, A., 2020. Late evolution of the inner Northern Apennines from the structure of the Monti del Chianti-Monte Cetona ridge (Tuscany, Italy). Journal of Structural Geology 141, 104205. https://doi.org/10.1016/j.jsg.2020.104205

Brogi, A., Cerboneschi, A., 2007. Upper crust «boudinage» during post-collisional Miocene extension in Tuscany: insights from the southern part of the Larderello geothermal area (Northern Apennines, Italy). Geodin. Acta 20 (5), 327–351.

Brogi A., Liotta, D., 2008. Highly extended terrains, lateral segmentation of the substratum, and basin development: the middle-late Miocene Radicondoli Basin (inner northern Apennines, Italy). Tectonics 27, 1–20.

Brogi, A., Lazzarotto, A., Liotta, D., Ranalli, G., 2005. Crustal structures in the geothermal areas of southern Tuscany (Italy): insights from the CROP 18 deep seismic reflection lines. J. Volcanol. Geotherm. Res. 148, 60–80.

Brunet, C., Monié, P., Jolivet, L., Cadet, J.-P., 2000. Migration of compression and extension in the Tyrrhenian Sea, insights from $^{40}Ar/^{39}Ar$ ages on micas along a transect from Corsica to Tuscany. Tectonophysics 321, 127–155.

Cabassi, J., Venturi, S., Di Bennardo, F., Nisi, B., Tassi, F., Magi, F., Ricci, A., Picchi, G., Vaselli, O., 2021. Flux measurements of gaseous elemental mercury (GEM) from the geothermal area of “Le Biancane” natural park (Monterotondo Marittimo, Grosseto, Italy): Biogeochemical processes controlling GEM emission. Journal of Geochemical Exploration 228, 106824.

Caine, S.J., Forster, C.B. 1999. Fault zone architecture and fluid flow: insight from field data and numerical modeling. In: Haneberg, W.C., Mozley, P.S., Moore, J.C. & Goodwin, L.B. (eds) Faults and Subsurface Fluid Flow in the Shallow Crust. geophysical Monographs, American geophysical Union, 113, 101–127.

Caine, J.S., Evans, I.P., Forster, C.B., 1996. Fault zone architecture and permeability structure. Geology 24, 1025–1028.

Calcagnile, G., Panza, G.F., 1980. The main characteristics of the Lithosphere Asthenosphere System in Italy and surrounding regions. Pure Appl. Geophys. 119, 865–879.

Camarda, M., Gurrieri, S., Valenza, M., 2006. CO_2 flux measurements in volcanic areas using the dynamic concentration method: influence of soil permeability. J. Geophys. Res. 111, B05202.

Camarda, M., De Gregorio, S., Favara, R., Gurrieri, S., 2007. Evaluation of carbon isotope fractionation of soil CO2 under an advective–diffusive regimen: A tool for computing the isotopic composition of unfractionated deep source. Geochimica et Cosmochimica Acta, 71, 3016-3027.

Camarda, M., Gurrieri, S., Valenza, M., 2009. Effects of soil gas permeability and recirculation flux on soil CO_2 flux measurements performed using a closed dynamic accumulation chamber. Chemical Geology 265, 387-393.

Camarda, M., De Gregorio, S., Capasso, G., Di Martino, R.M.R., Gurrieri, S., Prano, V., 2019. The monitoring of natural soil CO_2 emissions: Issues and perspectives. Earth Sci. Rev. 198, 102928.

Cameli, G.M., Dini, I., Liotta, D., 1993. Upper crustal structure of the Larderello geothermal field as a feature of post collisional extensional tectonics (Southern Tuscany, Italy). Tectonophysics 224, 413–423.

Cameli, G.M., Dini, I., Liotta, D., 1998. Brittle/ductile boundary from seismic reflection lines of southern Tuscany (Northern Apennines, Italy). Mem. Soc. Geol. It. 52, 153–163.

Capasso, G., D'Alessandro, W., Favara, R., Inguaggiato, S., Parello, F., 2001. Kinetic isotope fractionation of CO_2 carbon due to diffusion processes through the soil. In: Cidu, R. (Ed.), Proc. 10th Internat Symp. Water-Rock Interaction, pp. 1497–1499.

Carapezza, M.L., Federico, C., 2000. The contribution of fluid geochemistry to the volcano monitoring of Stromboli. Journal of Volcanology and Geothermal Research, 95, 227-245.

Carapezza, M.L., Ranaldi, M., Gattuso, A., Pagliuca, N.M., Tarchini, L., 2015. The sealing capacity of the cap rock above the Torre Alfina geothermal reservoir (Central Italy) revealed by soil CO_2 flux investigations. Journal of Volcanology and Geothermal Research 291, 25–34.

Cardellini, C., Chiodini, G., Frondini, F., Avino, R., Bagnato, E., Caliro, S., Lelli, M., Rosiello, A., 2017. Monitoring diffuse volcanic degassing during volcanic unrests: the case of Campi Flegrei (Italy). Scientific Reports 7, 6757.

Carmignani, L., Decandia, F.A., Fantozzi, P.L., Lazzarotto, A., Liotta, D., Meccheri, M., 1994. Tertiary extensional tectonics in Tuscany (northern Apennines, Italy). Tectonophysics 238, 295–315.

Chiodini, G., Cioni, R., Guidi, M., Raco, B., Marini, L., 1998. Soil CO_2 flux measurements in volcanic and geothermal areas. Appl. Geochem., 13 (1998), pp. 543-552.

Chiodini, G., Avino, R., Brombach, T., Caliro, S., Cardellini, C., De Vita, S., Frondini, F., Granieri, D., Marotta, E., Ventura, G., 2004. Fumarolic and diffuse soil degassing west of Mount Epomeo, Ischia, Italy. Journal of Volcanology and Geothermal Research 133, 291–309.

Chiodini, G., Baldini, A., Barberi, F., Carapezza, M.L., Cardellini, C., Frondini, F., Granieri, D., Ranaldi, M., 2007. Carbon dioxide degassing at Latera caldera (Italy): geothermal reservoir and evaluation of its potential energy. Journal of Geophysical Research 112, 17.

Chiodini, G., Caliro, S., Cardellini, C., Avino, R., Granieri, D., Schmidt, A., 2008. Carbon isotopic composition of soil CO_2 efflux, a powerful method to discriminate different sources feeding soil CO_2 degassing in volcanic-hydrothermal areas. Earth and Planetary Science Letters 274, 372–379.

Chiodini, G., Cardellini, C., Lamberti, M.C., Agusto, M., Caselli, A., Liccioli, C., Tamburello, G., Tassi, F., Vaselli, O., Caliro, S., 2015. Carbon dioxide diffuse emission and thermal energy release from hydrothermal systems at Copahue–Caviahue Volcanic Complex (Argentina). Journal of Volcanology and Geothermal Research 304, 294–303.

Costantini, A., Lazzarotto, A., Liotta, D., Mazzanti, R., Mazzei, R., Salvatorini, G., 2002. Note Illustrative Della Carta Geologica d'Italia Alla Scala 1:50.000-Foglio 306 Massa Marittima. L.A.C. Firenze 172 pp.

Cox, S.F., Knackstedt, M.A., Braun, J., 2001. Principles of structural control on perme- ability and fluid flow in hydrothermal systems. Rev. Economic Geology 11, 1–24.

Curewitz, D., Karson, J.A., 1997. Structural settings of hydrothermal outflow: Fracture permeability maintained by fault propagation and interaction. Journal of Volcanology and Geothermal Research 79, 149-168.

David, M., 1977. Geostatistical Ore Reserve Estimation. Elsevier Science, New York, p. 384.

De Matteis, R., Vanorio, T., Zollo, A., Ciuffi, S., Fiordelisi, A., Spinelli, E., 2008. Three-dimensional tomography and rock properties of the Larderello-Travale geothermal area. Italy. Phys. Earth Plan. Int. 168, 37–48.

Della Vedova, B., Bellani, S., Pellis, G., Squarci, P., 2001. Deep temperatures and surface heat flow distribution. In: Vai, G.B., Martini, I.P. (Eds.), Anatomy of an Orogeny: the Apennines and Adjacent Mediterranean Basins. Kluwer Academic Publishers, Dordrecht, pp. 65–76.

Delsarte, I., Cohen, G.J.V., Momtbrun, M., Höhener, P., Atteia, O., 2021. Soil carbon dioxide fluxes to atmosphere: The role of rainfall to control CO_2 transport. Applied Geochemistry 127, 104854.

Dershowitz, W.S., Herda, H.H., 1992. Interpretation of fracture spacing and intensity. 33rd U.S. Symposium on Rock Mechanics (USRMS), Santa Fe, New Mexico, June 1992. Paper Number: ARMA-92-0757.

Di Stefano, R., Bianchi, I., Ciaccio, M.G., Carrara, G., Kissling, E., 2011. Three-dimensional Moho topography in Italy: new constraints from receiver functions and controlled source seismology. Geochemistry, Geophysics, Geosystems 12 (9), 1–15.

Dini, A., Gianelli, G., Puxeddu, M., Ruggieri, G., 2005. Origin and evolution of Pliocene–Pleistocene granites from the Larderello geothermal field (Tuscan Magmatic Province, Italy). Lithos 81, 1–31.

Dini, A., Westerman, D.S., Innocenti, F., Rocchi, S., 2008. Magma Emplacement in a Transfer Zone: the Miocene Mafic Orano Dyke Swarm of Elba Island 302. Geological Society London Special Publications, Tuscany, Italy, 131–148.

Duchi, V., Minissale, A.A., Rossi, R., 1986. Chemistry of thermal springs in the Larderello-Travale geothermal region, southern Tuscany, Italy. Applied Geochemistry 1, 659-667.

Duchi, V., Minissale, A.A., Manganelli, M., 1992. Chemical composition of natural deep and shallow hydrothermal fluids in the Larderello geothermal field. Journal of Volcanology and Geothermal Research 49, 313-328.

Elter, M., Pandeli, E., 1990. Alpine and Variscan orogenic phases in the basement rocks of the Northern Apennines (Larderello geothermal field, Southern Tuscany, Italy). Eclogae Geol. Helv. 83, 241–264.

Elter, P., Giglia, G., Tongiorgi, M., Trevisan, L., 1975. Tensional and compressional areas in the recent (Tortonian to Present) evolution on northern Apennines. Boll. Geofis. Teor. Appl. 65, 3–18.

Fariley, J.P., Hinds, J.J., 2004. Rapid transport pathways for geothermal fluids in an active Great Basin fault zone. Geology 32, 825–828.

Faulds, J.E., Coolbaugh, M.F., Hinz, N.H., Cashman, P.H., Kratt, C., Dering, G., Edwards, J., Mayhew, B., McLachlan, H., 2011. Assessment of favorable structural settings of geothermal systems in the Great Basin, western USA. Geothermal Resources Council Transactions 35, 777–784.

Faulkner, D.R., Jackson, C.A.L., Lunn, R.J., Schlische, R.W., Shipton, Z.K., Wibberley, C.A.J., Withjack, M.O., 2010. A review of recent developments concerning the structure, mechanisms and fluid flow properties of fault zones. J. Struct. Geol. 32, 1557–1575.

Federico, C., Corso, P.P., Fiordilino, E., Cardellini, C., Chiodini, G., Parello, F., Pisciotta, A., 2010. CO_2 degassing at La Solfatara volcano (Phlegrean Fields): Processes affecting $\delta^{13}C$ and $\delta^{18}O$ of soil CO_2. Geochimica et Cosmochimica Acta 74, 3521-3538.

Fischer, T.P., Aiuppa, A., 2020. AGU Centennial Grand Challenge: Volcanoes and Deep Carbon Global CO_2 Emissions From Subaerial Volcanism—Recent Progress and Future Challenges. Geochemistry, Geophysics, Geosystems 21, e2019GC008690.

Fisher, R. A., 1953. Dispersion on a sphere. Proceedings of the Royal Society of London. Series A. Mathematical and Physical Sciences, 217 (1130), 295-305

Fridriksson, T., Bjarni Reyr, K., Halld´or, A., Eygerður, M., Snj´olaug, ´O., Chiodini, G., 2006. CO_2 emissions and heat flow through soil, fumaroles, and steam heated mud pools at the Reykjanes geothermal area, SW Iceland. Applied Geochemistry 21 (9), 1551–91569.

Frondini, F., Caliro, S., Cardellini, C., Chiodini, G., Morgantini, N., 2009. Carbon dioxide degassing and thermal energy release in the Monte Amiata volcanic-geothermal area (Italy). Applied Geochemistry 24, 860–875.

Gherardi, F., Panichi, C., Gonfiantini, R., Magro, G., Scandiffio, G., 2005. Isotope systematics of C-bearing gas compounds in the geothermal fluids of Larderello, Italy. Geothermics 34, 442-470.

Giammanco, S., Melián, G., Neri, M., Hernández, P.A., Sortino, F., Barrancos, J., López, M., Pecoraino, G., Perez, N.M., 2016. Active tectonic features and structural dynamics of the summit area of Mt. Etna (Italy) revealed by soil CO_2 and soil temperature surveying. Journal of Volcanology and Geothermal Research 311, 79–98.

Gola, G., Bertini, G., Bonini, M. Botteghi, S., Brogi, A., De Franco, R., Dini, A., Donato, A., Gianelli, G., Liotta, D., Manzella, A., Montanari, D., Montegrossi, G., Petracchini, L., Ruggieri, G., Santilano, A., Scrocca, D., Trumpy, E., 2017. Data integration and conceptual modelling of the Larderello geothermal area, Italy. Energy Procedia, 125, 300–309.

Golder Associated Ltd., 2009. Derivation of Basic Fracture Properties. Golder Associates Ltd., Portland, USA.

Gudjónsdóttir, S.R., Ilyinskaya, E., Hreinsdóttir, S., Bergsson, B., Pfeffer, M.A., Michalczewska, K., Aiuppa, A., Óladóttir, A.A., 2020. Gas emissions and crustal deformation from the Krýsuvík high temperature geothermal system, Iceland. Journal of Volcanology and Geothermal Research 391, 106350.

Hadgu, T., Karra, S., Kalinina, E., Makedonska, N., Hyman, J. D., Klise, K., Viswanathan, H.S., Wang, Y., 2017. A comparative study of discrete fracture network and equivalent continuum models for simulating flow and transport in the far field of a hypothetical nuclear waste repository in crystalline host rock. Journal of Hydrology, 553, 59-70.

Harvey, M.C., Rowland, J.V., Chiodini, G., Rissmann, C., Bloomberg, S., Hernández, P.A., Mazot, A., Viveiros, F., Werner, C., 2015. Heat flux from magmatic hydrothermal systems related to availability of fluid recharge. Journal of Volcanology and Geothermal Research 302, 225–236.

Hernández, P.A., Pérez, N.M., Fridriksson, T., Jolie, E., Ilyinskaya, E., Thárhallsson, A., Ívarsson, G., Gíslason, G., Gunnarsson, I., Jónsson, B., Padrón, E., Melián, G., Mori, T., Notsu, K., 2012. Diffuse volcanic degassing and thermal energy release from Hengill volcanic system, Iceland. Bulletin of Volcanology 74, 2435–2448.

Hooker, P.J., Bertrami, R., Lombardi, S., O'Nions, R.K., Oxburgh, E.R., 1985. Helium-3 anomalies and crust-mantle interaction in Italy. Geochimica et Cosmochimica Acta 49, 2505-2513.

Jentsch, A., Jolie, E., Jones, D.G., Taylor-Curran, H., Peiffer, L., Zimmer, M., Lister, B., 2020. Magmatic volatiles to assess permeable volcano-tectonic structures in the Los Humeros geothermal field. Mexico. Journal of Volcanology and Geothermal Research 394, 106820.

Jentsch, A., Duesing, W., Jolie, E., Zimmer, M., 2021. Monitoring the response of volcanic CO_2 emission to changes in the Los Humeros hydrothermal system. Scientific Reports 11, 17972.

Jolie, E., Klinkmueller, M., Moeck, I., 2015. Diffuse surface emanations as indicator of structural permeability in fault-controlled geothermal systems. Journal of Volcanology and Geothermal Research 290, 97–113.

Jolie, E., Klinkmueller, M., Moeck, I., Bruhn, D., 2016. Linking gas fluxes at Earth's surface with fracture zones in an active geothermal field. Geology, 44 (3), 187–190, doi:10.1130/G37412.1

Kim, Y.S., Peacock, D.C.P., Sanderson, D.J., 2004. Fault damage zones. Journal of Structural Geology, 26, 503-517.

Klusman, R.W., Moore, J.N., LeRoy, M.P., 2000. Potential for surface gas flux measurements in exploration and surface evaluation of geothermal resources. Geothermics 29, 637-670.

Korneva, I., Cilona, A., Tondi, E., Agosta, F., Giorgioni, M., 2015. Characterisation of the permeability anisotropy of Cretaceous platform carbonates by using 3D fracture modeling: the case study of Agri Valley fault zones (southern Italy). Ital. J. Geosci., Vol. 134, No. 3, 396-408.

Krige, D.G., 1951. A statistical approach to some basic mine valuation problems on the Witwatersrand. Journal of the Southern African Institute of Mining and Metallurgy 52, 119–139.

Labeur, A., Beaudoin, N. E., Lacombe, O., Emmanuel, L., Petracchini, L., Daëron, M., Klimowicz, S., Callot, J. P., 2021. Burial-deformation history of folded rocks unraveled by fracture analysis, stylolite paleopiezometry and vein cement geochemistry: a case study in the Cingoli Anticline (Umbria-Marche, Northern Apennines). Geosciences, 11(3), 135.

Lamberti, M.C., Vigide, N., Venturi, S., Agusto, M., Yagupsky, D., Winocur, D., Barcelona, H., Velez, M.L., Cardellini, C., Tassi, F., 2019. Structural architecture releasing deep-sourced carbon dioxide diffuse degassing at the Caviahue–Copahue Volcanic Complex. Journal of Volcanology and Geothermal Research 374, 131–141.

Lamberti, M.C., Chiodi, A., Agusto, M., Filipovich, R., Massenzio, A., Báez, W., Tassi, F., Vaselli, O., 2021. Carbon dioxide diffuse degassing as a tool for computing the thermal energy release at Cerro Blanco Geothermal System, Southern Puna (NW Argentina). Journal of South American Earth Sciences 105, 102833.

Lazzarotto, A., 1967. Geologia della zona compresa fra l'alta valle del Fiume Cornia ed il torrente Pavone (provincia di Pisa e Grosseto). Mem. Soc. Geol. Ital. 6, 151–197.

Lazzarotto, A., Mazzanti, R., 1978. Geologia dell'alta Val Di Cecina. Boll. Soc. Geol. Ital. 95, 1365–1487.

Leila, M., Lévy, D., Battani, A., Piccardi, L., Šegvić, B., Badurina, L., Pasquet, G., Combaudon, V., Moretti, I., 2021. Origin of continuous hydrogen flux in gas manifestations at the Larderello geothermal field, Central Italy. Chemical Geology 585, 120564.

Lelli, M., Raco, B., 2017. A reliable and effective methodology to monitor CO_2 flux from soil: The case of Lipari Island (Sicily, Italy). Applied Geochemistry 85, 73–85.

Lewicki, J.L., Bergfeld, D., Cardellini, C., Chiodini, G., Granieri, D., Varley, N., Werner, C., 2005. Comparative soil CO_2 flux measurements and geostatistical estimation methods on Masaya volcano, Nicaragua. Bulletin of Volcanology 68, 76-90.

Lewicki, J.L., Hilley, G.E., 2009. Eddy covariance mapping and quantification of surface CO_2 leakage fluxes. Geophysical Research Letters 36, L21802.

Liotta, D., 1991. The Arbia-Val Marecchia Line, Northern Apennines. Eclogae Geol. Helv. 84, 413–430.

Liotta, D., Brogi, A., 2020. Pliocene-Quaternary fault kinematics in the Larderello geo- thermal area (Italy): Insights for the interpretation of the present stress field. Geothermics 83, 101714.

Liotta, D., Ranalli, G., 1999. Correlation between seismic reflectivity and rheology in extended lithosphere: southern Tuscany, Inner Northern Apennines, Italy. Tectonophysics 315, 109–122.

Liotta, D., Cernobori, L., Nicolich, R., 1998. Restricted rifting and its coexistence with compressional structures: results from the Crop03 traverse (Northern Apennines, Italy). Terra Nova 10, 16–20.

Locardi, E., Nicolich, R., 1988. Geodinamica del Tirreno e dell'Appennino centro-meridionale: la nuova carta della Moho. Mem. Soc. Geol. Ital., 41, 121-140

Lubenow, B.L., Fairely, J.P., Lindsey, C.R., Larson, P.B., 2016. Influences on shallow ground temperatures in high flux thermal systems. Journal of Volcanology and Geothermal Research 323, 53-61.

Lucia, F.J., 1999. Carbonate Reservoir Characterization. Springer-Verlag, New York, USA. 336 pp.

Magro, G., Ruggieri, G., Gianelli, G., Bellani, S., 2003. Helium isotopes in paleofluids and present-day fluids of the Larderello geothermal field: Constraints on the heat source. Journal Of Geophysical Research 108, B1.

Manzella, A., Bonciani, R., Allansdottir, A., Botteghi, S., Donato, A., Giamberini, S., Lenzi, A., Paci, M., Pellizzone, A., Scrocca, D., 2018. Environmental and social aspects of geothermal energy in Italy. Geothermics 72, 232-248.

Martini, I.P., Sagri, M., 1993. Tectono-sedimentary characteristics and the genesis of the recent magmatism of Southern Tuscany and Northern Latium. Per. Mineral. 56, 157–172.

Martini, I., Ambrosetti, E., Brogi, A., Aldinucci, M., Zwaan, F., Sandrelli, F., 2021. Polyphase extensional basins: interplay between tectonics and sedimentation in the Neogene Siena-Radicofani Basin (Northern Apennines, Italy). International Journal of Earth Sciences 110(5), 1729–1751. 10.1007/s00531-021-02038-4.

Mason, E., Edmonds, M., Turchyn, A.V., 2017. Remobilization of crustal carbon may dominate volcanic arc emissions. Science 357, 290–294.

Matheron, G., 1970. The theory of regionalized variables and its applications. Fascicule n. 5, Les Cahiers du Centre De Morphologie Mathématique, Ecole des Mines de Paris, Fontainebleau 211.

Minissale, A., 1991. The Larderello geothermal field: a review. Earth Sciences Reviews, 31. 133-151.

Minissale, A., Evans, W.C., Magro, G., Vaselli, O., 1997. Multiple source components in gas manifestations from north-central Italy. Chemical Geology 142, 175-192.

Moeller, S., Grevemeyer, I., Ranero, C. R., Berndt, C., Klaeschen, D., Sallarès, V., Zitellini, N., de Franco, R., 2013. Early-stage rifting of the northern Tyrrhe- nian Sea Basin: Results from a combined wide-angle and multichannel seismic study. Geochemistry, Geophysics, Geosystems, 14(8), 3032–3052. https://doi.org/10.1002/ggge.20180

Molli, G., 2008. Northern Apennine–Corsica orogenic system: an updated overview. Geological Society, London, Special Publications 298, 413–442.

Nelson, R.A., 2001. Geologic Analysis of Naturally Fractured Reservoirs. Gulf Professional Publishing, 332 pp.

Nisi, B., Vaselli, O., Marchev, P., Tassi, F., 2013. Diffuse CO_2 soil flux measurements at the youngest volcanic system in Bulgaria: the 12.2 Ma old Kozhuh cryptodome. Acta Vulcanologica 25, 169–178.

Nisi, B., Vaselli, O., Tassi, F., Elio, J., Ortega, M., Caballero, J., Rappuoli, D., Mazadiego, L.F., 2014. Origin of the gases released from the Acqua Passante and Ermeta wells (Mt. Amiata, central Italy) and possible environmental implications for their closure. Annals of Geophysics, 57, S0438.

Oda, M., 1985. Permeability tensor for discontinuous rock masses. Géotechnique, vol. 35 (4), 483-495.

Orlandi, P., 2006. Siti di interesse minerario e mineralogico della Provincia di Pisa. Piano Territoriale di Coordinamento Approvato con Deliberazione di Consiglio Provinciale n. 100 del 27/07/2006. (In Italian).

Pandeli, E., Bertini, G., Castellucci, P., 1991. The tectonic wedges complex of the Larderello area (southern Tuscany, Italy). Boll. Soc. Geol. Ital. 110, 621–629.

Pandeli, E., Gianelli, G., Puxeddu, M., Elter, F.M., 1994. The paleozoic basement of the northern Apennines: stratigraphy, tectono-metamorphic evolution and alpine hydrothermal processes. Mem. Soc. Geol. Ital. 48, 627–654.

Parkinson K. J., 1981. An improved method for measuring soil respiration in the field. Journal of Applied Ecology 18, 221-228.

Pauselli, C., Gola, G., Mancinelli, P., Trumpy, E., Saccone, M., Manzella, A., and Ranalli, G., 2019, A new surface heat flow map of the Northern Apennines between latitudes 42.5 and 44.5 N. Geothermics 81, p. 39–52.

Peiffer, L., Carrasco-Núñez, G., Mazot, A., Villanueva-Estrada, R.E., Inguaggiato, C., Bernard-Romero, R., Rocha Miller, R., Rojas, J.H., 2018. Soil degassing at the Los Humeros geothermal field (Mexico). Journal of Volcanology and Geothermal Research 356, 163–174.

Pérez, N.M., Padilla, G.D., Padrón, E., Hernández, P.A., Melián, G.V., Barrancos, J., Dionis, S., Nolasco, D., Rodríguez, F., Calvo, D., Hernández, I., 2012. Precursory diffuse CO_2 and H_2S emission signatures of the 2011–2012 El Hierro submarine eruption, Canary Islands. Geophys. Res. Lett. 39, L16311.

Queißer, M., Burton, M., Kazahaya, R., 2019. Insights into geological processes with CO_2 remote sensing – a review of technology and applications. Earth Sci. Rev. 188, 389–426. https://doi.org/10.1016/j.earscirev.2018.11.016.

Raich, J.W., Schlesinger, W.H., 1992. The global carbon dioxide flux in soil respiration and its relationship to vegetation and climate. Tellus 44B, 81–99.

Regione Toscana, 2014. Supplemento al Bollettino Ufficiale della Regione Toscana n. 13 del 2.4.2014. Allegato A. (In Italian).

Rissmann, C., Christenson, B., Werner, C., Leybourne, M., Cole, J., Gravley, D., 2012. Surface heat flow and CO_2 emissions within the Ohaaki hydrothermal field, Taupo Volcanic Zone, New Zealand. Applied Geochemistry 27, 223–239.

Rochira, F., Caggianelli, A., De Lorenzo, S., 2018. Regional thermo-rheological field related to granite emplacement in the upper crust: Implications for the Larderello area (Tuscany, Italy). Geodinamic Acta, 30, 225–240.

Rolleau, E., Bravo, F., Pinti, D.L., Barde-Cabusson, S., Pizarro, M., Tardani, D., Muñoz, C., Sanchez, J., Sano, Y., Takahata, N., de la Cal, F., Esteban, C., Morata, D., 2017. Structural controls on fluid circulation at the Caviahue-Copahue Volcanic Complex (CCVC) geothermal area (Chile-Argentina), revealed by soil CO_2 and temperature, self-potential, and helium isotopes. Journal of Volcanology and Geothermal Research 341, 104–118.

Romagnoli, P., Arias, A., Barelli, A., Cei, M., Casini, M., 2010. An updated numerical model of the Larderello–Travale geothermal system, Italy. Geothermics 39, 292–313.

Rossetti, F., Faccenna, C., Jolivet, L., Goffé, B., Funiciello, R., 2002. Structural signature and exhumation P-T-t paths of the blueschist units exposed in the interior of the Northern Apennine chain, tectonic implications. Boll. Soc. Geol. Ital. 1, 829–842.

Rowland, J.V., Sibson, R.H., 2004. Structural controls on hydrothermal flow in a segmented rift system Taupo Volcanic Zone, New Zealand. Geofluids 4, 259–283.

Sbrana, A., Marianelli, P., Belgiorno, M., Sbrana, M., Ciani, V., 2020. Natural CO_2 degassing in the Mount Amiata volcanic–geothermal area. Journal of Volcanology and Geothermal Research 397, 106852.

Scandiffio, G., Panichi, C., Valenti, M., 1995. Geochemical evolution of fluids in the Larderello geothermal field. In: Proceedings of the Geothermal Congress 1995, 18–31 May, Florence, Italy (E. Barbier et al. eds.), 1839-1843.

Serri, G., Innocenti, F., Manetti, P., 2001. Magmatism from Mesozoic to Present: petrogenesis, time-space distribution and geodynamic implications. In: Vai, G.B., Martini, I.P. (Eds.), Anatomy of an Orogen: The Apennines and Adjacent Mediterranean Basins. Kluwer Academic Publishers, Amsterdam, pp. 77–103.

Serri, G., Innocenti, F., Manetti, P., 1993. Geochemical and petrological evidence of the subduction of delaminated Adriatic continental lithosphere in the genesis of the Neogene-Quaternary magmatism of central Italy. Tectonophysics 223, 117–214.

Sharp, Z.D., 2017. Principles of Stable Isotope Geochemistry. 2nd edition.

Sibson, R.H., 2000. Fluid involvement in normal faulting. In: In: Cello, G., Tondi, E. (Eds.), The Resolution of Geological Analysis and Models for Earthquake Faulting Studies J. Geodynam. 29, 469–499.

Silvestri, M., Marotta, E., Buongiorno, M.F., Avvisati, G., Belviso, P., Bellucci Sessa, E., Caputo, T., Longo, V., De Leo, V., Teggi, S., 2020. Monitoring of Surface Temperature on Parco delle Biancane (Italian Geothermal Area) Using Optical Satellite Data, UAV and Field Campaigns. Remote Sensing 12, 2018.

Sinclair, A.J., 1974. Selection of threshold values in geochemical data using probability graphs. Journal of Geochemical Exploration 3, 129–149.

Snow, D. T., 1965. A parallel plate model of fractured permeable media. University of California, Berkeley.

Spiess, R., Langone, A., Caggianelli, A., Stuart, F.M., Zucchi, M., Bianco, C., Brogi, A., Liotta, D., 2021. Unveiling ductile deformation during fast exhumation of a granitic pluton in a transfer zone. Journal of Structural Geology 147, 104326.

Tassi, F., Fiebig, J., Vaselli, O., Nocentini, M., 2012. Origins of methane discharging from volcanic-hydrothermal, geothermal and cold emissions in Italy. Chemical Geology 310–311, 36–48.

Tassi, F., Nisi, B., Cardellini, C., Capecchiacci, F., Donnini, M., Vaselli, O., Chiodini, G., 2013. Diffuse soil emission of hydrothermal gases (CO_2, CH_4, and C_6H_6) at Solfatara crater (Campi Flegrei, southern Italy). Applied Geochemistry 35, 142–153.

Tassi, F., Cabassi, J., Calabrese, S., Nisi, B., Venturi, S., Capecchiacci, F., Giannini, L., Vaselli, O., 2016. Diffuse soil gas emissions of gaseous elemental mercury (GEM) from hydrothermal-volcanic systems: an innovative approach by using the static closed-chamber method. Applied Geochemistry, 66, 234–241.

Taussi, M., Nisi, B., Pizarro, M., Morata, D., Veloso, E.A., Volpi, G., Vaselli, O., Renzulli, A., 2019. Sealing capacity of clay-cap units above the Cerro Pabellón hidden geothermal system (northern Chile) derived by soil CO_2 flux and temperature measurements. Journal of Volcanology and Geothermal Research 384, 1–14.

Taussi, M., Nisi, B., Vaselli, O., Maza, S., Morata, D., Renzulli, A., 2021. Soil CO_2 and temperature from a new geothermal area in the Cordón de Inacaliri Volcanic Complex (Northen Chile). Geothermics 89, 101961.

Terzaghi, R., 1965. Sources of Error in Joint Surveys. Géotechnique, 15, 287-304.

Theye, T., Reinhardt, J., Goffé, B., Jolivet, L., & Brunet, C., 1997. Ferro-and magnesiocarpholite from the Monte Argentario (Italy): First evidence for high-pressure metamorphism of the metasedimentary Verrucano sequence, and significance for PT path reconstruction. European Journal of Mineralogy, 859-874.

Vai, G.B., Martini, I.P., 2001. Anatomy of an Orogen: the Apennines and Adjacent Mediterranean Basins. Kluwer Academic, Dordrecht, 2001.

Venturi, S., Tassi, F., Bicocchi, G., Cabassi, J., Capecchiacci, F., Capasso, G., Vaselli, O., Ricci, A., Grassa, F., 2017. Fractionation processes affecting the stable carbon isotope signature of thermal waters from hydrothermal/volcanic systems: The examples of Campi Flegrei and Vulcano Island (southern Italy). Journal of Volcanology and Geothermal Research 345, 46–57.

Venturi, S., Tassi, F., Magi, F., Cabassi, J., Ricci, A., Capecchiacci, F., Caponi, C., Nisi, B., Vaselli, O., 2019. Carbon isotopic signature of interstitial soil gases reveals the potential role of ecosystems in mitigating geogenic greenhouse gas emissions: case studies from hydrothermal systems in Italy. Science of the Total Environment 655, 887–898.

Viveiros, F., Cardellini, C., Ferreira, T., Caliro, S., Chiodini, G., Silva, C., 2010. Soil CO_2 emissions at Furnas volcano, São Miguel Island, Azores archipelago: Volcano monitoring perspectives, geomorphologic studies, and land use planning application. Journal of Geophysical Research 115, B12208.

Viveiros, F., Chiodini, G., Cardellini, C., Caliro, S., Zanon, V., Silva, C., Rizzo, A.L., Hipólito, A., Moreno, L., 2020. Deep CO_2 emitted at Furnas do Enxofre geothermal area (Terceira Island, Azores archipelago). An approach for determining CO_2 sources and total emissions using carbon isotopic data. Journal of Volcanology and Geothermal Research 401, 106968.

Volatili, T., Agosta, F., Cardozo, N., Zambrano, M., Lecomte, M., Tondi, E., 2022. Outcrop-scale fracture analysis and seismic modelling of a basin-bounding normal fault in platform carbonates, central Italy. Journal of Structural Geology, 155, 104515.

Wei, Z. Q., Egger, P., Descoeudres, F., 1995. Permeability predictions for jointed rock masses. In: International Journal of Rock Mechanics and Mining Sciences and Geomechanics Abstracts 32, 3, 251-261.

Werner, C., Cardellini, C., 2006. Comparison of carbon dioxide emissions with fluid upflow, chemistry, and geologic structures at the Rotorua geothermal system, New Zealand. Geothermics 35, 221–238.

Werner, C., Bergfeld, D., Farrar, C.D., Doukas, M.P., Kelly, P.J., Kern, C., 2016. Decadal-scale variability of diffuse CO_2 emissions and seismicity revealed from long-term monitoring (1995–2013) at Mammoth Mountain, California, USA. Journal of Volcanology and Geothermal Research 289, 1, 51-63

Whiticar, M.J., 1999. Carbon and hydrogen isotope systematics of bacterial formation and oxidation of methane. Chemical Geology 161, 291–314.

Zambrano, M., Tondi, E., Korneva, I., Panza, E., Agosta, F., Janiseck, J. M., Giorgioni, M., 2016. Fracture properties analysis and discrete fracture network modelling of faulted tight limestones, Murge Plateau, Italy. Italian Journal of Geosciences, 135(1), 55-67.

Zambrano, M., Pitts, A.D., Salama, A., Volatili, T., Giorgioni, M., Tondi, E., 2019. Analysis of Fracture Roughness Control on Permeability Using SFM and Fluid Flow Simulations: Implications for Carbonate Reservoir Characterization. Geofluids, vol. 2019, 4132386.

Zhang, D., Zhang, R., Chen, S., Soll, W.E., 2000. Pore scale study of flow in porous media: scale dependency, REV, statistical REV. Geophys. Res. Lett. 27, 1195-1198.

Zucchi, M., Brogi, A., Liotta, D., Rimondi, V., Ruggieri, G., Montegrossi, G., Caggianelli, A., Dini, A., 2017. Permeability and hydraulic conductivity of faulted micaschist in the eastern Elba Island exhumed geothermal system (Tyrrhenian sea, Italy): insights from Cala Stagnone. Geothermics 70, 125–145.

Zucchi, M., Brogi, A., Liotta, D., Caggianelli, A., Dini, A., Ventruti, G., Ruggieri, G., Matera, PF. 2022. Fractures, fluid flow and inherited structures in geothermal systems: inputs from the Fe-ore deposits of eastern Elba Island (Northern Apennines, Italy). Geological Magazine, 1-24. https://doi.org/10.1017/ S0016756822000310.